

The parallelism between galaxy clusters and early-type galaxies:

III. The Mass-Radius Relationship

C. Chiosi¹, M. D’Onofrio^{1,*}, E. Merlin², L. Piovan¹ and P. Marziani³

¹ Department of Physics and Astronomy, University of Padova, Vicolo Osservatorio 3, I35122, Italy
e-mail: cesare.chiosi@unipd.it, mauro.donofrio@unipd.it, lorenzo.piovan@gmail.com

² INAF - Astronomical Observatory of Rome, Via Frascati 33, I00078 Monte Porzio Catone (RM), Italy
e-mail: emiliano.merlin@inaf.it

³ INAF - Astronomical Observatory of Padua, Vicolo Osservatorio 5, I35122, Italy
e-mail: paola.marziani@inaf.it

Received June 20, 2020; accepted July 20, 2020

ABSTRACT

Context. This is the third study of a series dedicated to the observed parallelism of properties between Galaxy Clusters and Groups (GCGs) and early-type galaxies (ETGs).

Aims. Here we investigate the physical origin of the Mass-Radius Relation (MRR).

Methods. Having collected literature data on masses and radii for objects going from Globular Clusters (GCs) to ETGs and GCGs, we set up the MR-plane and compare the observed distribution with the MRR predicted by theoretical models both for the monolithic and hierarchical scenarios.

Results. We argue that the distributions of stellar systems in the MR-plane is due to complementary mechanisms: (i) on one hand, as shown in paper II, the relation of the virial equilibrium does intersect with a relation that provides the total luminosity as a function of the star formation history; (ii) on the other hand, the locus predicted for the collapse of systems should be convolved with the statistical expectation for the maximum mass of the halos at each cosmic epoch. This second aspect provides a natural boundary limit explaining either the curved distribution observed in the MR-plane and the existence of a zone of avoidance.

Conclusions. The distribution of stellar systems in the MR-plane is the result of two combined evolution, that of the stellar component and that of the halo component.

Key words. Clusters of galaxies – Early-type galaxies – structure – photometry – scaling relations – simulations

1. Introduction

In recent years, much attention has been paid to the Mass-Radius Relationship (MRR) of galaxies, the early-type galaxies (ETGs) in particular. The MRR is indeed basic to any theory of galaxy formation and evolution. To this aim, an impressive body of data have been acquired concerning the masses and dimensions of galaxies and galaxy clusters and groups not only in the local old Universe but also in the distant and young one, thus making it feasible to address the question whether these two important parameters changed with time as predicted by any hierarchical mode of galaxy formation, see for instance the studies by Shankar et al. (2011), Bernardi et al. (2011), Graham (2011, 2013), Bernardi et al. (2014), Agertz & Kravtsov (2016), Kuchner et al. (2017), Huang et al. (2017), Somerville et al. (2018), Genel et al. (2018), Terrazas et al. (2019), and references therein.

The subject of the MRR of galaxies from ETGs to dwarf ellipticals and dwarf spheroidals (dwarf galaxies, DGs, in general), including also bulges and Globular Clusters (GCs) has been reviewed by Graham (2011, 2013) to whom we refer for many details. The current MRRs for ETGs and DGs will be presented below. At the same time data for the mass and radius of Galaxy Clusters and Groups (GCGs) have been acquired (see for

instance Valentinuzzi et al. 2011; Cariddi et al. 2018, WINGS data, and references therein). Therefore, it is worth of interest to investigate whether a similar MRR exists for this class of objects and how it would compare with the one of galaxies.

In addition to this, convincing evidence has been gathered that at relatively high redshifts, objects of mass comparable to that of nearby massive galaxies but with smaller dimensions exist. These “compact galaxies” are found up to $z \geq 3$ with stellar masses from 10^{10} to $10^{12} M_{\odot}$ and half-light radii from 0.4 to 5 kpc (i.e. 3 to 4 times more compact than the local counterparts of the same mass), and in nearly similar proportions there are galaxies with the same mass but a variety of dimensions (e.g., Mancini et al. 2009; Valentinuzzi et al. 2010), and bulge to disk ratios (e.g., Karim et al. 2011). However, here we want to start considering only the case of standard ETGs and GCGs, leaving the compact galaxies aside.

In D’Onofrio et al. (2019b) (hereafter paper II) we have already analyzed the origin of the scaling relations from the point of view of the stellar component. We have demonstrated that these relations originate from the combination of the virial theorem with the luminosity evolution of the galaxies. The aim of this study is instead that of looking at the general physical principles governing in particular the MRR.

We will address in particular the question: why do GCGs, ETGs and GCs obey a rather narrow MRR instead of scattering around showing a broader combination of these two parameters?

* Corresponding author

Similar analyses have been made by Chiosi & Carraro (2002) and Chiosi et al. (2012), so that the present study is a sequel of those ones motivated by the better data nowadays at our disposal. To clarify the aims and the methods of the present study (and also the previous ones), we anticipate here the essence of the analysis. We speculate that the observed MRR is the result of two complementary mechanisms: (i) Objects from GCs to ETGs and GCGs crowd on the MR-plane along loci with the same slope but different zero points. We name these loci model MRRs (M-MRRs). They are parameterized by the initial density (redshift) at which these proto-systems collapse. The slopes of the M-MRRs are about a factor of two flatter than the observational MRR. The M-MRRs are scarcely affected by the dominant formation mechanism at work, either quasi-monolithic or hierarchical. Furthermore, along each mass sequence, the evolutionary history of the massive galaxies tend to reach the ideal case of the dissipationless collapse, whereas the less massive ones significantly depart from this. (ii) At each redshift the mass distribution galactic halos is set by cosmology, i.e. there is the upper mass limit for collapsed objects. This implies a limit to the mass extension of each M-MRR of the manifold, i.e. a boundary line on the MR-plane, the slope of which changes with the mass (roughly more than a factor of two on logarithmic scale for masses and radii). The galaxies along this boundary are in mechanical and thermal equilibrium. If a galaxy does not meet these conditions, its position on the MR-plane is above the boundary line. The intersection of the M-MRR manifold with the boundary lines at different redshift yields the observed MRR for objects going from GCs to GCGs.

The paper is subdivided as follows. In Section 2 we present and discuss the observational MRR for three samples of galaxies and galaxy clusters. In Section 3 we shortly describe the hydrodynamical models of galaxies (and clusters) over a large range of masses contained in the large scale simulations by (Vogelsberger et al. 2014a,b; Genel et al. 2014; Nelson et al. 2015) that are adopted here as the main source of theoretical data¹. In Section 3 we derive the theoretical MRR from the large scale simulations both for the present day Universe and as function of the redshift and try to highlight the main causes determining the observational MRR. In Section 4 based on elementary theories of cosmology and galaxy formation we derive the same MRR and compare it with that obtained from the large scale simulation showing that good agreement exists. In Section 5 we seek to derive the MRR from First Principles highlighting the deep causes that eventually determine its shape. Finally, in Section 6 we draw some remarks and conclusions.

Throughout the paper we assumed in all our calculations the same values of the Λ -CDM cosmology used in the Illustris simulations by Vogelsberger et al. (2014a,b): $\Omega_m = 0.2726$, $\Omega_\Lambda = 0.7274$, $\Omega_b = 0.0456$, $\sigma_8 = 0.809$, $n_s = 0.963$, $H_0 = 70.4 \text{ km s}^{-1} \text{ Mpc}^{-1}$.

2. The observational Mass-Radius Relation

In this section we present the data for single galaxies and galaxy clusters and groups. These are: (i) the catalog of ETGs, spiral galaxies, DGs, GCs and GCGs in the Local Group and local Universe by Burstein et al. (1997); (ii) the SDSS data for ETGs by Bernardi et al. (2010) roughly covering the redshift interval $z=0$ to ≈ 2 ; (iii) the samples of ETGs, Bright Cen-

¹ The more recent data of Illustris-TNG have not been included in the present study to secure homogeneity with the previous ones of the series.

tral Galaxies (BCGs) and GCGs set up by Valentinuzzi et al. (2011); Cariddi et al. (2018) using the data of the WINGS survey; (iv) finally, the list of dwarf galaxies for the local Group is supplemented by that of Woo et al. (2008), Geha et al. (2006), Hamraz et al. (2019), and that of galactic GCs of Burstein et al. (1997) by the data of Pasquato & Bertin (2008) and the transition objects from GCs to DGs of Kissler-Patig et al. (2006).

The Burstein et al. (1997) data. Over the years these very popular data have been examined by many authors so that a detailed presentation is superfluous here. We limit ourselves to show in Fig. 1 the distribution on the $\log R_s$ vs $\log M_s$ plane of the various subgroups of the data set from the classical GCs to GCGs: the red filled circles are the ETGs, the green open circles the spiral galaxies crowding the same area but not considered in the analysis, the blue triangles the dwarf galaxies, the red squares the globular clusters, finally the light-blue filled squares the ETG-rich and Sp-rich Clusters/Groups all together. The best fit of the sole ETGs yields for $M_s \geq 10^{10} M_\odot$

$$\log R_s = (0.59 \pm 0.01) \log M_s - (5.85 \pm 0.16) \quad (1)$$

where M_s (in M_\odot) is the estimated stellar mass and R_s (in kpc) is the radius containing half of it (nearly identical to the classical effective radius R_e), $rms = 0.13$ and the correlation parameter $corr = 0.91$. This relation is taken from Chiosi & Carraro (2002) who used the same data. This line is then extended to the domain of GCs and of GCGs, however arbitrarily shifted by -0.1 dex on both coordinates, to highlight the role of this line as a border of the observed distribution of astrophysical objects whose mass extends over about eleven orders of magnitude (the blue dashed line).

The ETGs of Bernardi et al. (2010). A much richer sample of data for ETGs has been derived by Bernardi et al. (2010) from the SDSS catalog. The sample contains $\approx 60,000$ galaxies² The observational MRR is displayed in Fig. 1, the green filled circles. The linear best fit of the SDSS data is

$$\log R_s = (0.537 \pm 0.001) \log M_s - (5.26 \pm 0.01) \quad (2)$$

where M_s and R_s have their usual meaning and units (the magenta dashed line), $rms = 0.094$ and the correlation parameter $corr = 0.89$. The slope (and zero point) of the above MRR is quite robust as nearly coincides with similar determinations made by other authors: e.g. Chiosi & Carraro (2002) using the Burstein et al. (1997) data and Shen et al. (2003) using the SDSS data. We will show that the same slope is also recovered using the Illustris simulations.

The distribution of the bulk of galaxies is confirmed by the smaller sample of Shankar et al. (2011) also extracted from the SDSS survey but using slightly different selection criteria. The area covered by the observational data is slightly larger than the one with the Bernardi et al. (2010) data.

The WINGS database. In recent times, large optical and spectroscopic databases for the galaxy content of nearby clusters have become available thanks to the Wide-field Nearby Galaxy-cluster Survey (WINGS) of Fasano et al. (2006) and Varela et al. (2009) and companion OMEGA-WINGS extension of Gullieuszik et al. (2015) and Moretti et al. (2017) for a number of clusters in the redshift interval ($0.04 \leq z \leq 0.07$). All

² The selection conditions are $\text{fracDeV} = 1$ and $b/a > 0.6$, therefore the sample is dominated by elliptical galaxies (see Bernardi et al. (2010) for more details).

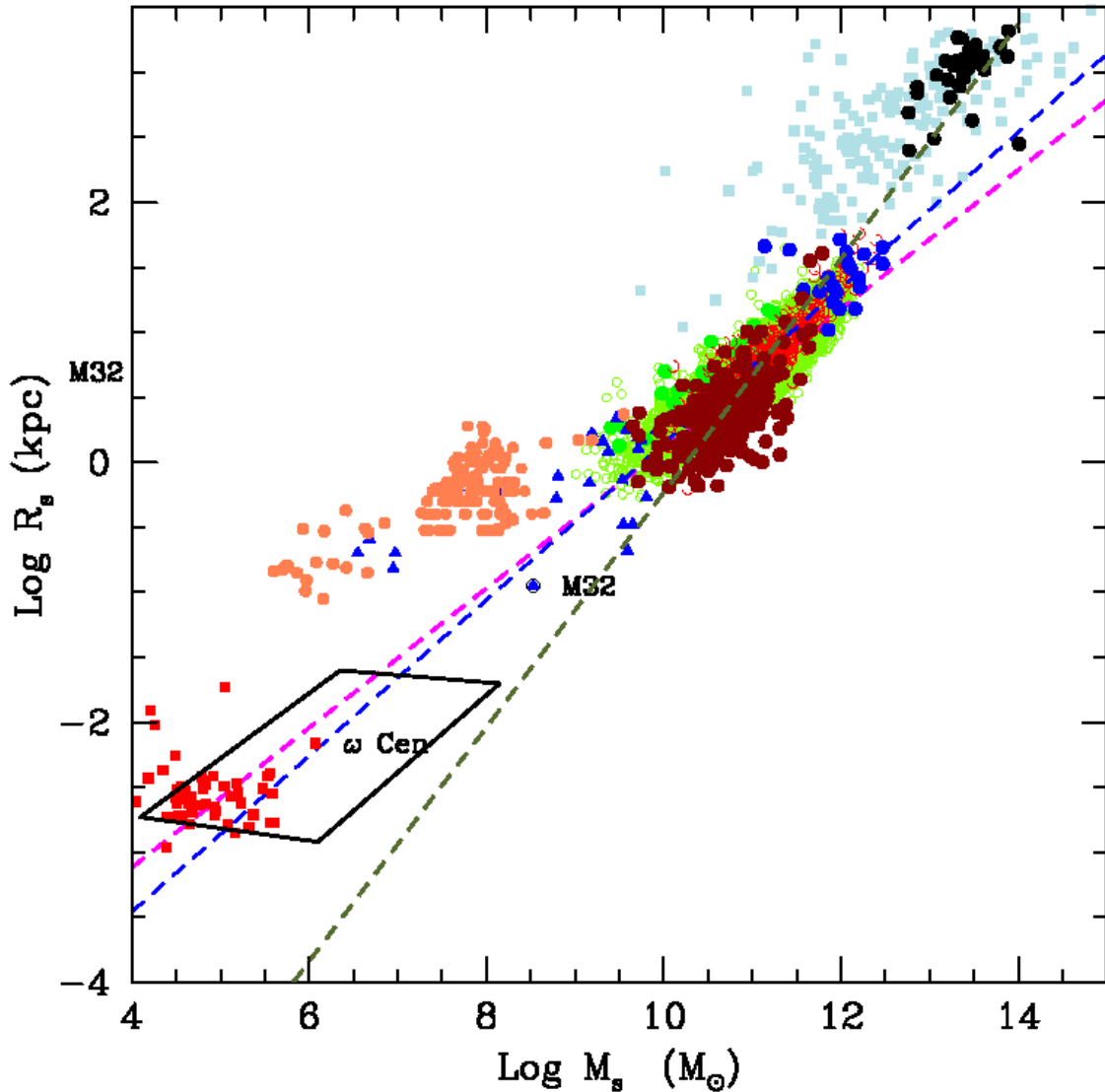


Fig. 1. The $\log(R_s)$ versus $\log(M_s)$ relation for all the samples under consideration. R_s is the half-mass radius, and M_s the total stellar mass. Although R_s is not strictly identical to the effective radius R_e , they are very close to each other. Throughout this paper we will always use R_s , which is easier to calculate for hydrodynamical models of galaxies, and assume $R_s \approx R_e$. Burstein et al. (1997) sample: the filled red circles are the ETGs, the green open circles the SGs, the blue filled triangles the DGs, the filled red squares the GCs, the filled light-blue squares the GCGs. The blue dashed line is the linear best fit of eqn. (1), i.e. $\log R_s = 0.60 \log M_s - 5.859$ relative to the sole ETGs, however extended to the regions of GCs and GCGs. Bernardi et al. (2010) sample: only ETGs are present indicated by green filled circles. The dashed magenta line is the linear best fit of the data extended to GCs and GCGs. WINGS sample: the dark-red filled circles are the ETGs, the blue filled circles the BCGs, and the black filled circles the GCGs. The olive-green dashed line is the linear best-fit of all WINGS objects together $\log(R_s) = 0.901 \log M_s - 9.245$, however extended to DGs and GCs. Dwarf galaxies and Globular Clusters: the coral filled circles are the DGs of Woo et al. (2008) and Geha et al. (2006) all together. Finally, the parallelogram shows the area occupied by the transition objects from GCs to DGs of Kissler-Patig et al. (2006).

this material has been subsequently examined by Cariddi et al. (2018) with particular attention to the problems of the accurate determination of the stellar light and the stellar mass profiles of galaxy clusters. WINGS measured and examined thousand of galaxies in 46 clusters, providing the absolute V and B magnitudes, the morphological types (according to the classification system RC3; de Vaucouleurs et al. (1991), Corwin et al. (1994) and Fasano et al. (2012)), four different estimates of the star formation rates (SFR) and the estimates of the stellar masses M_s (Fritz et al. 2007, 2011) and the effective radii R_e and effective surface brightness (D’Onofrio et al. 2014). The issue of the membership of the galaxies to the clusters under consideration

has been addressed and examined by Cava et al. (2009) to whom we refer for all details. In this study we have considered all the 46 clusters studied by Cariddi et al. (2018). The MR-plane of this set of data is shown in Fig. 1 where the dark-red filled circles are the ETGs, the blue filled circles the BCGs, and the black filled circles the GCGs. The inspection of the WINGS data reveals that: (i) compared to Burstein et al. (1997) and Bernardi et al. (2010) at given mass the radii of ETGs are smaller by about 0.3 dex whereas those of BCGs and GCGs are comparable; (ii) the MRR relation for the ETGs more massive than $10^{10} M_\odot$ is

$$\log R_s = (0.46 \pm 0.04) \log M_s - (4.60 \pm 0.40) \quad (3)$$

where masses and radii are in the usual units, $rms = 0.22$ and $cor = 0.61$; (iii) the scatter around this reference MRR is much larger than in the previous cases; (iv) ETGs and Spirals crowd in the same region of the MR-plane; (v) extended plumes at the large mass side of the MRR may exist only for ETGs belonging to clusters and not for ETGs belonging to the field and in general not for both field and cluster late type galaxies (D’Onofrio et al. 2019b); (vi) looking at the cluster ETGs, the MRR has curved banana-like shape with a well developed plume toward high masses and radii made of red galaxies as confirmed by their B-V color and also their Sérsic index n (D’Onofrio et al. 2019a). In contrast, in field ETGs the banana-like structure of the MRR and the red plume is much less evident if not missing at all. The reason for this striking difference is not clear, most likely it is related to the higher probability for massive cluster ETGs of merging and/or engulfing other galaxies of smaller mass in the case of wet mergers to avoid any bluing effect in their colors or of comparable mass and age in case of dry mergers among similar objects thus leaving the color unchanged (see the discussion in Sciaratta et al. 2019).

Considering all the objects together (ETGs, BCGs and GCGs) the MRR is

$$\log R_s = (0.90 \pm 0.01) \log M_s - (9.24 \pm 0.18) \quad (4)$$

with $rms = 0.28$ and $cor = 0.95$ (the dark olive-green dashed line in Fig. 1). It is worth noting that adopting eq. (4) as the actual MRR for galaxies and galaxy clusters and basing on its slope, one might conclude that the observed MRR simply mirrors the slope of 1 expected from the virial equilibrium condition (D’Onofrio et al. 2019b). In this study we will show that in reality the MRR owns its origin to a more complicate interplay among different causes.

Dwarf Galaxies. The DGs are taken from different sources: (i) the Burstein et al. (1997) sample of dEs and dSphs of the Local Group (indicated as B-DGs). It is worth recalling that the masses used by Burstein et al. (1997) are the dynamical masses and not the stellar masses, so this group is not strictly homogeneous with the sample for ETGs; (ii) the sample of DGs by Geha et al. (2006) (indicated as G-DGs); (iii) the DGs of the Local Group according to the measurements made by Woo et al. (2008) (indicated as W-DGs). Fortunately, all the three samples of data yield much similar MRRs

$$\log R_s = (0.22 \pm 0.05) \log M_s - (2.1 \pm 0.5) \quad (5)$$

$$\log R_s = (0.22 \pm 0.07) \log M_s - (1.9 \pm 0.5) \quad (6)$$

$$\log R_s = (0.28 \pm 0.03) \log M_s - (2.4 \pm 0.2) \quad (7)$$

Eq.(5) is for the B-DGs with $rms = 0.281$ and $cor = 0.632$, eq.(6) for the G-DGs with $rms = 0.193$ and $cor = 0.300$, and Eq.(7) for the W-DGs $rms = 0.201$ and $cor = 0.851$. Here we consider the three relationships as identical, but give more weight to that of Woo et al. (2008) with the highest correlation parameter. Finally, we take into account the study by Kissler-Patig et al. (2006) on the transition objects from GCs to dwarf galaxies. All these data are shown in Fig. 1.

Galaxy Clusters and Groups. Two sources of data for galaxy clusters and groups have been considered, namely Burstein et al. (1997) and the WINGS and Omega-WINGS database (Fasano et al. 2006; Varela et al. 2009; Cava et al. 2009; Moretti et al. 2014; D’Onofrio et al. 2014; Gullieszick et al. 2015; Moretti et al. 2017; Caminha et al. 2017; Cariddi et al. 2018). In particular the parameters R_s and M_s

needed to the present study are those measured by Caminha et al. (2017) and Cariddi et al. (2018). See also D’Onofrio et al. (2019a) for more details.

On the MRR slope. It is soon evident that there is no unique slope for the MRR of ETGs and DGs. The slope for ETGs goes from 0.5 to 0.6, and for dwarf galaxies from 0.217 to 0.272. Furthermore, looking at the data in detail, the slope is even steeper than 0.54 in the region of the largest and most massive ETGs going up to 1 and even more, see the top part of the MRR by Bernardi et al. (2010), Guo et al. (2009), van Dokkum et al. (2010), Graham (Fig. 1 in 2011) and Graham (2013). This is a point to keep in mind when interpreting the observational data.

General Remarks. Information and details on how the stellar masses M_s and half-mass radii, R_s , have been derived can be found in the original sources to which the reader should refer. Of course some possible systematic biases among the different sets of data are to be expected, whose entity, however, ought to be small. This is somewhat sustained by the overall agreement among different sources as far as some general relationships are concerned, e.g. the agreement in the slope of the MRR for ETGs between Bernardi et al. (2010) and Burstein et al. (1997). The same for the dwarf galaxies. However, since the groups of objects will be treated separately and only from a general qualitative point of view, no homogenization of the data is needed. Furthermore, despite the important remarks about the WINGS galaxies, we can say that there is no substantial difference passing from the MRR based on the Burstein et al. (1997) data, to the one based on the Bernardi et al. (2010) data, and finally the WINGS data. Our analysis of the MRR for ETGs (and partially spirals as well) will primarily stand on the SDSS sample of Bernardi et al. (2010), thus securing internal homogeneity of the mass and radius estimates. Finally, in this study the MRR derived from the Bernardi et al. (2010) data will be considered as the reference case.

3. Current theoretical models of galaxies and galaxy clusters

Our aim here is to present the numerical simulations of galaxies and clusters that we have used to interpret and reproduce the observed properties of real galaxies and clusters.

The primary source of data is the Illustris compilation³ (Vogelsberger et al. 2014a,b; Genel et al. 2014; Nelson et al. 2015, to whom we refer for all details), a suite of large, highly detailed cosmological hydrodynamical simulations, including star, galaxy and black-hole formation and tracking the expansion of the universe (Hinshaw et al. 2013). The procedure we have adopted to extract theoretical data from the Illustris database is amply described in D’Onofrio et al. (2019b) to whom the reader should refer for all details. Suffice to mention here that in order to follow the evolution of each galaxy we have extracted from the Illustris database the data of stellar mass, dark matter mass, total mass, luminosity, half-mass radius of the stellar component, velocity dispersion and star formation rate for the whole set of galaxies (with mass $\log(M_s) \geq 9$ at $z = 0$) in the selected clusters at the redshift $z = 0, z = 0.2, z = 0.6, z = 1, z = 1.6, z = 2.2, z = 3$ and $z = 4$. With these data we have analyzed the MRR at different epochs following the progenitors of each object.

In this section we present a quick analysis of the Illustris sample of galaxy models. Hereinafter M_D, R_D, M_B, R_B, M_s and R_s are masses and half-mass radii of Dark Matter (DM), Baryonic Matter (BM) made of stars and gas (initially only gas) and

³ <http://www.illustris-project.org/data/>

stellar mass (initially zero), respectively. The total mass of a galaxy is defined as $M_T = M_D + M_B$. At the beginning the ratio $M_D/M_B = \omega$ is fixed by the cosmological model of the Universe, in our case for Ω_m/Ω_b $\omega \simeq 5.92 \simeq 6$. It is worth keeping in mind that in the course of the formation and evolution processes the above masses can change in presence of galactic winds and/or stripping and/or acquisition of material by interactions with other galaxies or intergalactic medium.

3.1. Stars and DM: relationships among M_s , M_D , R_s and R_D

The relationships M_s vs M_D and R_s vs R_D for four different values of the redshift ($z=4, 2, 1$, and 0) are shown in the left and right panels of Fig. 2, respectively. Masses (in M_\odot) and radii (kpc) are in logarithmic notation and the color code indicates the redshift ($z=4$, blue; $z=2$, green; $z=1$, yellow; $z=0$, red).

The M_s vs M_D relationship. At the beginning of the galaxy formation history, DM ad BM are in cosmological proportions (i.e. $M_D = \omega M_B$ with $\omega \simeq 6$), but star formation gradually stores more and more baryonic mass into stars. It may be worth of interest to evaluate the efficiency of the star formation process over the Hubble time in galaxies of different mass. Since $M_B < M_D$ so M_s is always smaller than M_D . However, since galaxies of different total mass may build stars at different efficiencies, the ratio M_s to M_D is expected not to be constant, but to vary with M_D and redshift. In the left panel of Fig. 2, we note that M_s always increases with M_D so that low mass galaxies build up less stars with respect to the more massive ones, however the slope of the relation as the redshift goes to zero. In more detail, for redshifts ($z \gtrsim 2$) and masses $M_D \simeq 10^{12} M_\odot$ the slope decreases at decreasing redshift so that more and more stars are present at given M_D . More precisely, for ($z \lesssim 2$) and $M_D \leq 10^{12} M_\odot$ the above trend holds good to, but above this mass limit the opposite seems to occur, at given M_D less star mass is present than expected. In other words, massive galaxies are less efficient builders of their stellar content (the star formation is over). The relationship between $\log M_s$ and $\log M_D$ is $M_s = \alpha M_D + \beta$ and the best-fits are given in Table 1.

To quantify the efficiency of star formation we calculate the ratio M_s/M_D as a function of M_D . In this case we can neglect the change of slope in the M_s vs M_D relation above a certain value of M_D at low redshifts. Finally we get the inverse of M_s/M_D given by the expression

$$\frac{M_D}{M_s} = 10^{-\beta} M_D^{1-\alpha} \quad \text{and} \quad \frac{M_D}{M_s} = \omega \frac{M_B}{M_s} \quad (8)$$

where the ratio M_B/M_s measures how much of the original BM mass is turned into stars.

The values of $(1 - \alpha)$ and $-\beta$ are listed in Table 2 for the four redshifts we are considering.

For the sake of illustration we list in Table 3 the ratio M_s/M_D as a function of the total mass limited to the case of $z = 0$. In general the ratios M_s/M_D and M_s/M_B decrease with the total galaxy mass. Similar results were found by Chiosi & Carraro (2002), Merlin & Chiosi (2006, 2007) and Merlin et al. (2012) thus showing that old models were already able to catch the essence of the galaxy formation problem.

The R_s vs R_D relationship. In similar way we derive the relations $R_s = \eta R_D^\gamma$ that are shown in the right panel of Fig. 2 and the entries of Table 1 for the case of $z = 0$. The radius of R_D is more extended than R_s by a factor of about 3 to 10 as the galaxy mass increases from $10^9 M_\odot$ to $10^{13} M_\odot$. The slope γ of $R_s - R_D$ relation (logarithmic) first decreases by about a factor of two passing

Table 1. The M_s vs M_D and R_s vs R_D relations. For M_s vs M_D the analytical form is adopted: $\log M_s = \alpha \log M_D + \beta$ ($M_s = 10^\beta M_D^\alpha$). For R_s vs R_D the expression $\log R_s = \gamma \log R_D + \eta$ ($R_s = 10^\eta R_D^\gamma$) is used. Masses and radii are in M_\odot and kpc, respectively. The models are from the Illustris catalog.

z	M_s vs M_D			R_s vs R_D		
	α	β	M_D	γ	η	R_D
4	1.55	-8.19		0.39	-0.20	
2	1.44	-6.78		0.30	0.03	
1	1.16	-3.37	< 12.0	0.22	0.07	
	0.76	2.30	> 12.0	0.22	0.07	
0.	0.93	-0.43	< 11.5	0.296	-0.087	
	0.79	1.22	> 11.5	0.294	-0.042	

Table 2. Coefficients of the relationships $\log(M_D/M_s) = (1 - \alpha) \log M_D - \beta$ with at different redshifts. The data are taken from the Illustris catalog of model galaxies. Masses are in M_\odot .

Redshift	α	$-\beta$
4.0	-0.555	8.186
3.0	-0.498	7.514
2.0	-0.441	6.782
1.0	-0.100	2.927
0	0.093	0.229

Table 3. Efficiency of the star formation in galaxies of different mass observed at redshift $z = 0$. The efficiency is measured by the ratio M_s/M_D . The data are taken from the Illustris catalog of model galaxies. Masses are in M_\odot .

Redshift $z=0$					
M_D	M_B	M_T	$\log M_s$	$\frac{M_s}{M_D}$	$\frac{M_D}{M_s}$
10^{12}	$1.67 \cdot 10^{11}$	$1.167 \cdot 10^{12}$	10.770	0.058	17.12
10^{11}	$1.67 \cdot 10^{10}$	$1.167 \cdot 10^{11}$	9.863	0.073	13.71
10^{10}	$1.67 \cdot 10^9$	$1.167 \cdot 10^{10}$	8.852	0.089	11.17
10^9	$1.67 \cdot 10^8$	$1.167 \cdot 10^9$	8.057	0.114	8.77
10^8	$1.67 \cdot 10^7$	$1.167 \cdot 10^8$	7.162	0.145	6.88
10^7	$1.67 \cdot 10^6$	$1.167 \cdot 10^7$	6.267	0.182	5.48

from $z=4$ to $z=1$, and then increases again at $z=0$. What is more important is that while at high redshifts (our $z=4$, $z=2$ and $z=1$ cases) the galaxy distribution on the R_s vs R_D plane is a random cloud of points, at $z=0$ a regular trend gets in place in which R_s increases with R_D on the side of large values of R_D (largest masses). On the side of low values of both radii and masses a cloud of points is still there. The effect of this is to increase the mean slope of the whole distribution. What does it imply? We will try to cast light on this issue.

3.2. The R_s vs M_s relation at different redshifts

In Fig. 3 we show the R_s vs M_s relations of the Illustris models at the four values of the redshift considering (the color code we have adopted). Like the case of R_s vs R_D relations, the distribution is clumpy and irregular at high redshifts independently of the galaxy mass. Starting from $z=1$ and more evident at $z=0$ a tail-like feature develops at the side of large masses, say $\gtrsim 1 - 2 \cdot 10^{11} M_\odot$.

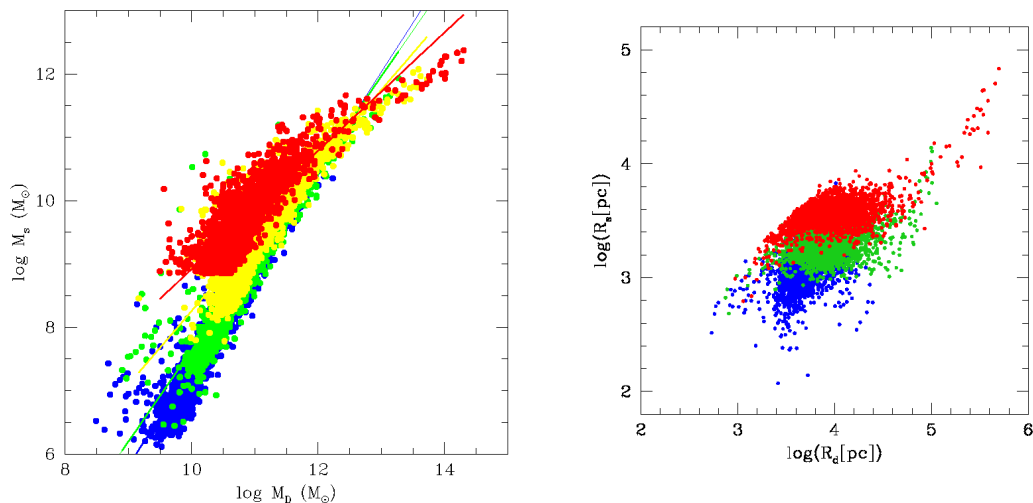


Fig. 2. **Left Panel:** The $M_s - M_D$ relations at different redshifts ($z=4$, blue; $z=2$, green; $z=1$, yellow; $z=0$, red). Masses are in solar units. The solid lines are the best fits, the coefficients of which are given in Table 1. **Right Panel:** the same as in the left panel but for the $R_s - R_D$ relations. Radii are in kpc.

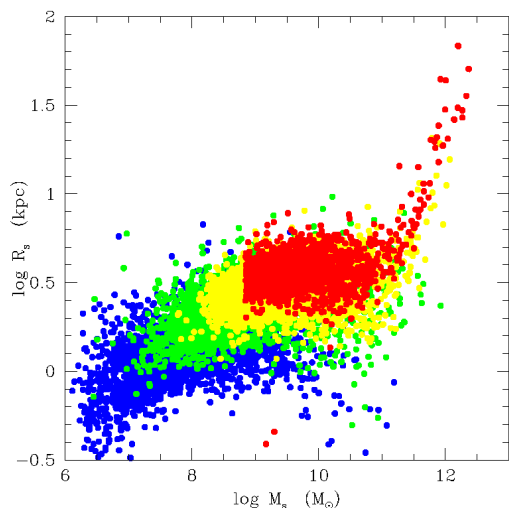


Fig. 3. The stellar half-mass radius R_s vs the mass M_s of the galaxy models of the Illustris database at different values of the redshift, i.e. $z=4$ (blue), $z=2$ (green), $z=1$ (yellow) and $z=0$ (red).

The best fit of the data at redshift $z=0$ using the relationship $R_s = \eta M_s^\epsilon$ (where masses and radii are in M_\odot and kpc, respectively) yields the values listed in Table 4. At higher redshifts, the tail at the side of large masses is much less evident if not missing at all. The tail seems to disappear starting from $z=1$. The R_s vs M_s relation is much similar to that of the low mass galaxies at $z=0$, i.e. nearly flat. At any value of the mass in the mass range of the data cloud, the dispersion in the radius is very large. At redshift $z=0$, the tail has slope and zero point much similar to those derived by Chiosi et al. (2012) using the SDSS data of Bernardi et al. (2010).

What is the reason for the cloud-like and tail-like distributions at low redshifts? Why the cloud-like one dominates in the low mass range and at high redshifts? The opposite trend happens for the tail-like one, which shows up in the high mass range and at low redshifts. What is the physical meaning of the two dis-

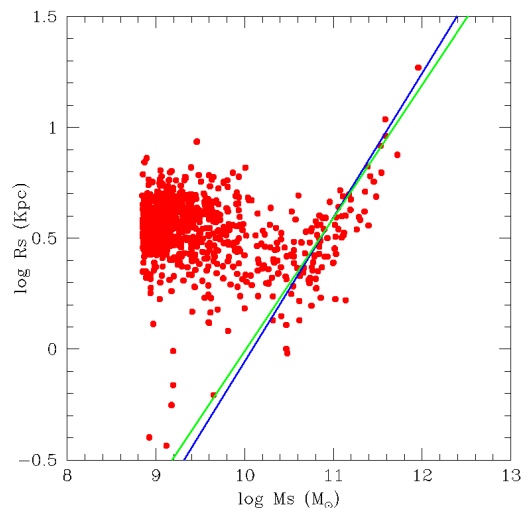


Fig. 4. The same of Fig. 3 but limited to the sample for $z=0$ for all models with null star formation rate.

Table 4. The radius-mass relation of the stellar component $R_s = \eta M_s^\epsilon$. Masses and radii are in M_\odot and kpc, respectively. Each relation is a two slopes one with separation mass $M_s = 2 \times 10^{11} M_\odot$ suggested by the data.

Case	$M_s \leq 2 \times 10^{11} M_\odot$		$M_s > 2 \times 10^{11} M_\odot$	
	ϵ	η	ϵ	η
Illustris	-0.005	0.592	0.651	-6.557
Chiosi et al. (2012)	0.187	-1.626	0.570	-5.694

tributions? To cast light on these issues we examine the history of the R_s vs M_s relation of a number of individual galaxies.

3.3. The detailed history of the R_s vs M_s relation for selected models

The Illustris simulations are based on the hierarchical scheme, therefore each galaxy is the result of a number of mass acquisition/removal processes, which change the masses M_D , M_s and the radii R_D and R_s of the galaxy. For each galaxy in the sample at $z=0$, the Illustris data base provides the past history, i.e. the masses and radii of the components sub-units during the Hubble time. This means that we can reconstruct the past history in the R_s vs M_s plane of each galaxy from $z=4$ to $z=0$. The path of each galaxy on the MR-plane is quite tortuous: We can summarize the complex situation as follows: in mergers among low mass objects the mass and the radius increase, however, exceptions are possible, where either the mass or the radius or both. In general the model galaxies remain inside the cloud-like region of the R_s vs M_s plane. Mergers among galaxies of relatively high mass tend to generate objects that shift outside the cloud and tend to fall close to a well behaved radius-mass sequence (actually they define it) and their locus agrees with the observational radius-mass relationship for ETGs (see e.g. Chiosi et al. 2012, and references therein). Finally, the cloud-like region coincides with the distribution of dwarf galaxies of different type (see the discussion by Chiosi & Carraro 2002). The MRR for massive galaxies is very close to the relation set by the condition of virial equilibrium (this issue will be examined in great detail below), so one might be tempted to conclude that systems that at the present time ($z=0$) that are able to satisfy the virial condition have the minimum energy and hence radius for their existing structure. Dwarf galaxies, most likely because they are undergoing active star formation, cannot be in this ideal condition. So the question arises spontaneously: do dwarf galaxies exist that fulfill the virial state? What determines the large radius of dwarf galaxies well visible in Fig. 1. Recasting the question in a different way: are there DGs whose position on the MR-plane is near the MRR of normal ETGs? In other words in conditions of mechanical and thermal equilibrium. The following considerations can be made.

Given the mass of a galaxy (either acquired by mergers or already in place “ab initio”), the radius mirrors the condition of mechanical equilibrium of the system. In other words it is a consequence of the energy balance between external dynamical processes (collapse) or internal feed-back by star formation and other sources. To answer the above question one should look at galaxies in which at least star formation activity has extinguished since a reasonable amount of time. To this aim we consider the $z=0$ sample (most likely containing many objects with null star formation) and isolate the galaxies with null star formation rate (SFR=0). These are plotted in Fig. 4 the galaxies with SFR=0 at $z = 0$. In addition to galaxies of high mass, there are also a few objects of low mass that fall very close to the prolongation of best-fit line of the Bernardi et al. (2010) ETGs (see Chiosi et al. 2012). Their observational counterparts could be objects like ω Cen and M32. So it seems that also low mass galaxies can exist sharing the same equilibrium conditions of the massive ones. This conclusion is however biased by the large uncertainties on the SFR, which is known only up to three decimal digits. A SFR of the order of $10^{-4} M_\odot/\text{yr}$ or lower cannot be neglected in the case of dwarf galaxies. This may explain why even for this case a residual cloud-like feature still remains.

3.4. Comparison between observations and theory

Before proceeding further, it is mandatory to compare the observational data with theoretical galaxy models in usage. This is shown in Fig. 5 which displays the following data: i) Burstein et al. (1997) sample of ETGs, DGs, GCGs, and GCs that is a fairly homogeneous set of sample. ii) Bernardi et al. (2010) of ETGs. This sample is by far more numerous than the previous one for galaxies of the same type. iii). The WINGS data for ETGs, BCGs and GCGs by Valentinuzzi et al. (2011); Cariddi et al. (2018). The emphasis here is given to the group of ETGs. The theoretical models are those of the hydrodynamical large scale simulations of the Illustris project Vogelsberger et al. (2014a,b) at redshift $z = 0$ (the olive green dots) in the pure hierarchical scheme, those by (Chiosi & Carraro 2002) in the pure monolithic scenario, and finally those by (Merlin & Chiosi 2006, 2007; Merlin et al. 2010, 2012; Chiosi et al. 2012) in the so-called early-hierarchical view, both at redshift $z = 0$. The emphasis is given to the Illustris models that are considered as the reference case. From this comparison we see that

i) The Burstein et al. (1997) data for ETGs fairly agree with the Illustris models of comparable mass. Unfortunately Illustris does not extend enough into the regions populated by DGs, simply because for technical reasons the sample at $z = 0$ is limited in mass at $10^9 M_\odot$. In addition to it, the observational sample to disposal contains too few DGs. Therefore, nothing can be said for this type of objects. As already note the MRR of ETGs given by eq. (1) has slope ≈ 0.6 , even though the most massive ETGs would be better represented by a slope ≈ 1 thus suggesting a MRR the slope of which slightly changes at increasing mass. For the moment we leave it aside. We will come back to it later on. This best-fit-line for ETGs, extended downward to the domain of GCs and upward to that of GCGs and vertically shifted by $\Delta \log R_s \approx 0.3$, would match all three groups of objects and leave all the data in the semi-plane above it.

The same considerations and results are derived from using the Bernardi et al. (2010), for which the best fit MRR of the sole ETGs is given by eq.(2), which is only slightly different from the previous one. They agree with the Burstein et al. (1997) data and the Illustris models. The extension of the ETGs’ MRR also hit the GCs and GCG.

The WINGS data all together suggest a steeper slope of the MRR, i.e. 0.95 ± 0.02 . The inclusion of galaxy clusters has forced the slope to higher values. Extending this relation (the solid line) to the domain of GCs would not match these objects. Furthermore, the WINGS data do not cover the region of galaxies with $M_s \approx 10^9 M_\odot$ so that they do not completely overlap the area reached by Illustris models. However, if we derive the MRR limited to the case of ETGs, the agreement between theory (Illustris) and data is remarkable and the best-fit line of the ETGs alone (dashed line) would hit the region of GCs.

The main conclusion of this mutual comparison between data from different sources and the theoretical models of Illustris is that all of them seem to fairly agree each other. As a matter of facts, different sources of observational data, different photometry, and different volume coverage of the space, but similar results. This is very important, because they suggest that the conclusions are not severely affected by the source of data in usage.

Finally, we proceed to compare theoretical models with other theoretical models. The black filled squares connected by the black line are the models by Chiosi & Carraro (2002) for low initial over-density with respect to the surrounding medium and different mass, whereas the red squares connected by the red line are models of the same type but different mass and very high

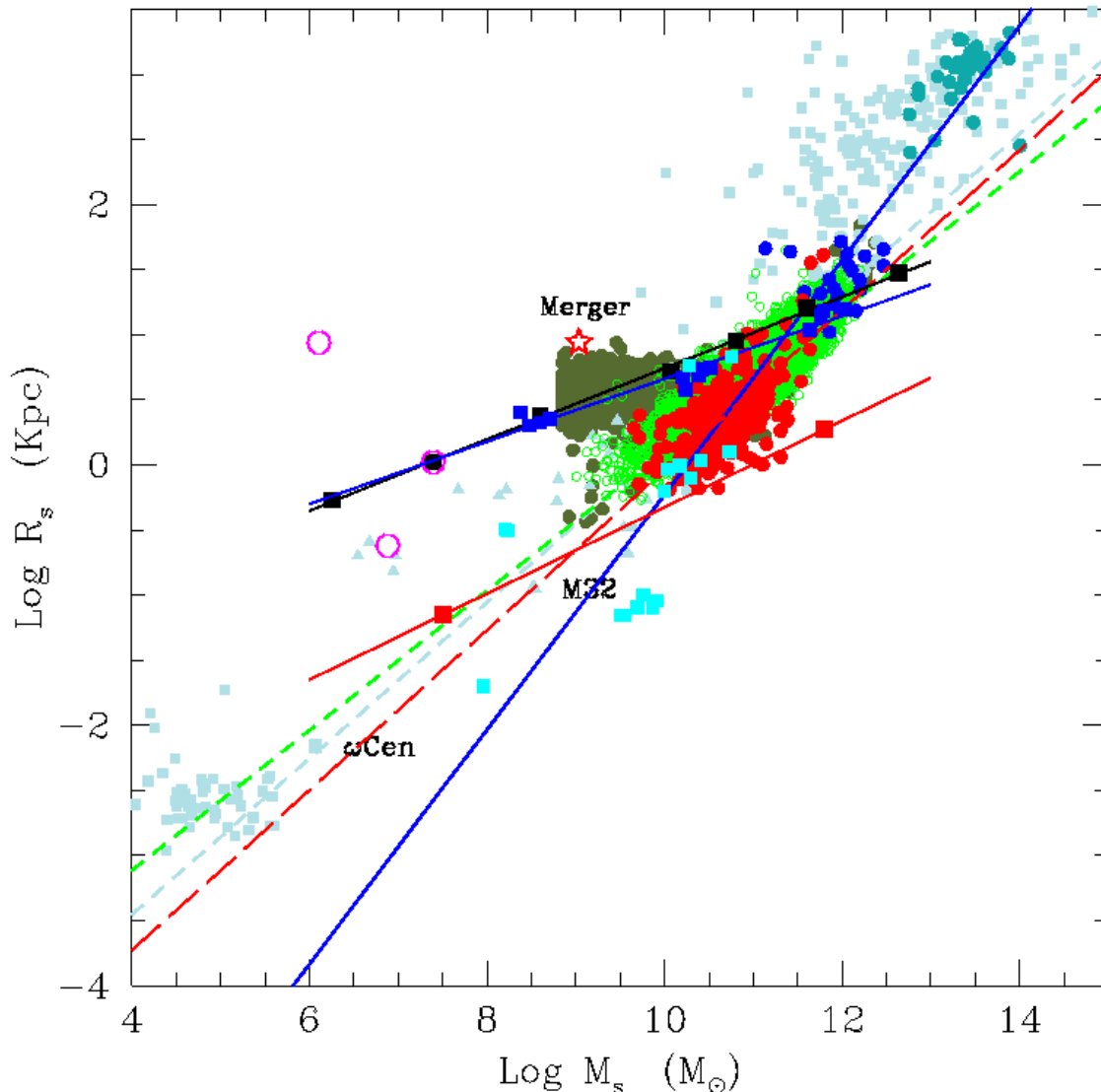


Fig. 5. The composite R_s vs M_s relation and comparison between theory and observations. The light powder-blue dots are the data of Burstein et al. (1997) for ETGs, DGs, GCs and GCGs: the dashed line of the same colour is the best fit of the sole ETGs however extended to the domains of GCs and GCGs. The bright green dots are the Bernardi et al. (2010) data for ETGs, and the thick dashed line of the same colour is the best-fit line of these latter. The red dots, blue dots, and green-blue dots are the ETGs, BCGs, and GCGs of the WINGS sample. The dashed red line is the best-fit line of the ETGs, whereas the solid blue line is the best fit of all WINGS data lumped together. The slope of this latter line is very close to MRR for virialized objects. In such case the line fails to hit the region of Globular Clusters. Finally, we display different theoretical models for comparison. The black filled squares and the black solid line are the monolithic models by Chiosi & Carraro (2002) and their linear fit. The three magenta open circles are low mass ETGs with the same mass but different initial densities by Chiosi & Carraro (2002). See the data of Table B.2. The empty red star is the case of merger reported by Chiosi & Carraro (2002). The blue squares and the blue line are the hierarchical models by Merlin et al. (2010, 2012), see Table B.3. The light blue-green squares are the ancillary model of Chiosi et al. (2012), see Table B.3. The dark live-green points are the reference model galaxies of the Illustris simulations.

initial over-density contrast. The three coral circles are monolithic models of the same mass ($10^9 M_\odot$) but different initial density contrast by Chiosi & Carraro (2002). The blue filled squares connected by the blue line are the models by Merlin et al. (2010, 2012). The cyan filled squares are incomplete models of different mass and initial over-density limited to the very first evolutionary stages calculated by Chiosi et al. (2012) according to the early hierarchical scheme. They were meant to localize the initial position of model galaxies on the MR-plane. Details on the input/output parameters of all the model galaxies are given in Table B.1, B.2, and B.3 of Appendix B. It is worth noting that the

slope of the MRR of the models at varying the mass but keeping constant the initial conditions (over-density) are very similar each other.

Remarkably, there is substantial agreement among the various types of models. Taking the Illustris case as a reference, the monolithic and early hierarchical models fall onto the same position on the MR-plane, the only difference being due to the richness of the three samples. While the Illustris models amount to more than 2500 cases of different mass (total and stellar) and initial conditions that are picked up from large scale simulations (see Vogelsberger et al. 2014a,b, for more details), those

by Chiosi & Carraro (2002) and Merlin & Chiosi (2006, 2007); Merlin et al. (2010, 2012); Chiosi et al. (2012) are much fewer in number and different way of defining the initial conditions. The Chiosi & Carraro (2002) models were designed and calculated one by one assuming the initial over-density of the proto-cloud with respect to the surrounding cosmological medium and the initial positions and velocities of the DM and BM particles. Those by Merlin & Chiosi (2006, 2007); Merlin et al. (2010, 2012); Chiosi et al. (2012) stem from mini-large-scale numerical cosmological simulations (about 10 Mpc by 10 Mpc) that allowed for repeated mergers among sub-clumps of DM and BM in the same field. In this respect they are somewhat similar to the models by Vogelsberger et al. (2014a,b). From this comparison, we also learn another important fact: at given total stellar mass M_s at the present time ($z = 0$) galaxies tend to have the same size R_s independently of the past formation history (pure monolithic, early hierarchical, pure hierarchical) because they share the same area of the MR-plane.

Furthermore, hydrodynamical simulations of galaxies that more or less share the same initial conditions tend to converge to the same locus on the MR-plane no matter of details in input physics and numerical technique. In contrast, models with the same total mass but different initial conditions converge to different loci on the MR-plane that however run parallel each other. Higher initial density objects tend to remain smaller in size during their whole life. Finally, from this comparison among different galaxy models we learn that also those obtained with modest computing resources and simplified physical input and numerical technique are fully adequate to explore a large variety of astrophysical problems.

The most important issues and questions raised by this section are (1) understanding the physical meaning of the line splitting the MR-plane in two regions: (a) the one containing the observational data for objects with mass spanning about ten orders of magnitude from GCs to GCGs; (b) the one void of objects with exception of the much fewer compact galaxies (see Chiosi et al. 2012, for a short discussion of the issue); (2) the fact that this line is unique and the separation is very sharp; (3) in principle galaxies of suitable mass and/or initial density could fall in the “forbidden semi-plane” but for some yet not clear reasons the vast majority of real galaxies do not. It is worth recalling that the “forbidden semi-plane” coincides with the region named “Zone of avoidance (ZOE) by Burstein et al. (1997). A plausible explanation of the “forbidden semiplane” has been advanced long ago by Chiosi & Carraro (2002) and Chiosi et al. (2012). Considering the recent wealthy of modern data and theoretical models, in the following we go over it again.

4. Theoretical predictions for the MRR

In this section, we examine the theoretical foundations of the MRR and highlight the possible physical causes of its occurrence.

4.1. The MRR of collapsing proto-galaxies made of DM + BM

Independently of the formation scheme (either monolithic or hierarchical) the seeds of galaxy structures are perturbations of matter made of DM and BM that undergo collapse when the density contrast with respect to the surrounding medium reaches

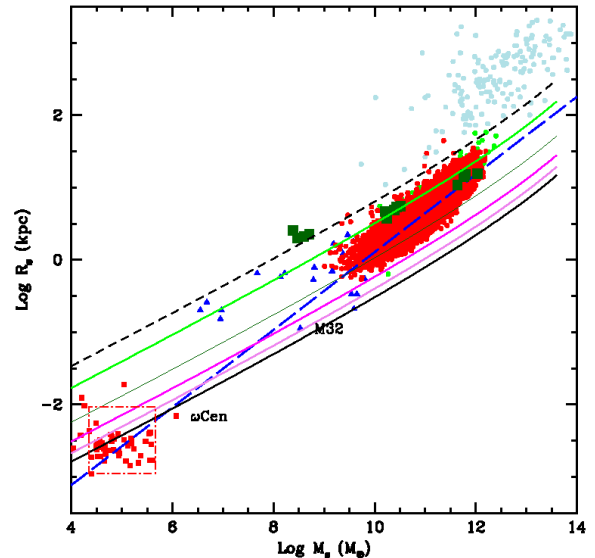


Fig. 6. Comparison of the Fan et al. (2010) lines and the theoretical models by Merlin et al. (2012) (green filled squares) with the observational data of Burstein et al. (1997) from GCs (small red squares), to DGs (small blue triangles), and GCGs (light blue filled circles) plus the ETGs of Bernardi et al. (2010) (red dots). The short-dashed blue line is the Fan et al. (2010) relation for $z = 0$. The solid thin lines of different colors are the same relation but for $z = 1$, $z = 5$, $z = 10$, $z = 15$, and $z = 20$, from top to bottom in the order. The long-dashed, thick blue line is the best-fit of the ETGs of Bernardi et al. (2010) extended to GCs and GCGs.

a suitable value. Assuming spherical symmetry for the sake of simplicity, the MRR for individual galaxies is given by

$$\left(\frac{4\pi}{3}\right)R_D^3 = \frac{M_D}{\lambda\rho_u(z)} \quad (9)$$

where $\rho_u(z) \propto (1+z)^3$ is the density of the Universe at the redshift z , and λ the factor for the density contrast of the DM halo. This expression is of general validity whereas the function λ depends on the cosmological model of the Universe, including the Λ -CDM case. All details and demonstration of it can be found in (Bryan & Norman 1998, their Eq. 6).

In the context of the Λ -CDM cosmology, Fan et al. (2010) have adapted the general relation (9) to provide an expression correlating the halo mass M_D and the star mass M_s of the galaxy born inside it, the half light (mass) radius R_s of the stellar component, the redshift at which the collapse takes place z_f , the shape of the BM galaxy via a coefficient $S_S(n_S)$ related to the Sersic brightness profile from which the half-light radius is inferred and the Sersic index n_S , the velocity dispersion of the BM component with respect to that of DM (expressed by the parameter f_σ), and finally the ratio $m = M_D/M_s$. The expression is

$$R_s = 0.9 \left(\frac{S_S(n_S)}{0.34}\right) \left(\frac{25}{m}\right) \left(\frac{1.5}{f_\sigma}\right)^2 \left(\frac{M_D}{10^{12}M_\odot}\right)^{1/3} \frac{4}{(1+z_f)}. \quad (10)$$

Typical value for the coefficient $S_S(n_S)$ is 0.34. Furthermore, f_σ yields the three dimensional star velocity dispersion as a function of the DM velocity dispersion, $\sigma_s = f_\sigma\sigma_{DM}$. Here we adopt $f_\sigma = 1$. For more details see Fan et al. (2010) and references therein.

The most important parameter of eq.(10) is the ratio $m = M_D/M_s$. Basing on the Illustris data we have investigated how this ratio varies in the mass interval $10^{8.5} < M_D < 10^{13.5}$ (masses are in M_\odot) and from $z = 0$ to $z = 4$ and made some predictions over a wider mass range $10^4 < M_D < 10^{15}$ and a wider redshift interval from $z = 0$ to $z = 10$. The analysis and results are presented in Appendix A where we confine $m(M_D, z)$ within a rather narrow range of possible values and suggest that a simple relationship giving the ratio m as a function of M_{DM} might be the one of eq.(A.5) that is repeated here for the sake of clarity

$$\log m = \log \frac{M_D}{M_s} = 0.062 \log M_D + 0.429$$

which turns out to be sufficiently accurate for a qualitative nature of our investigation. In a very recent study Girelli et al. (2020) have thoroughly investigated the stellar-to-halo mass ratio of galaxies ($M_s/M_{DM} = 1/m$ i.e. the inverse of our parameter m) in the mass interval $10^{11} < M_{DM} < 10^{15}$ and redshifts from $z = 0$ to $z = 4$. They have used a statistical approach to link the observed galaxy stellar mass function on the COSMOS field to the halo mass function from the Λ CDM-Dustgrain simulations and an empirical model to describe the variation of the stellar-to-halo mass ratio as a function of the redshift. Finally they provide analytical expressions for the function $m(M_D, z)$. Noting that in the mass interval in common their results are in substantial agreement with those inferred from the Illustris data, we prefer to provisionally adopt here eq. (A.5) for the sake of internal consistency with the theoretical galaxy models in usage.

We would like to point out that relation 10 is strictly valid only for monolithic infall of BM into collapsing DM potential wells. Nevertheless, this formula provides a general reference to obtain the typical dimension of a galactic system as a function of its mass and formation redshift. While adjustments are possible, the general trend is well defined. However, some deviations from this law are possible and expected, e.g. for low redshifts. See below for further discussion. The MR-plane of the hydrodynamical models and the loci expected for different redshift from eqn. (10) above are shown in Fig. 6 together with the ETGs by Bernardi et al. (2010).

The slope of relation (10) is nearly identical to the one estimated from the hydrodynamical models; the small difference can be fully ascribed to the complex baryon physics, which causes the stellar system to be slightly offset with respect to the locus analytically predicted from DM halos. Therefore, a model slope (close to 1/3) different from that of the observational MRR is not the result of inaccurate description of the physical processes taking place in a galaxy; on the contrary, it mirrors the fundamental relationship between mass and radius in any system of given mean density. Indeed it is remarkable that quite complicated numerical calculations clearly display this fundamental feature. *If this is the case, why do real galaxies gather along a line with a different slope?*

What is still missing in the above MRR is that galaxies (globular clusters and cluster of galaxies) form and evolve in a given cosmological scenario which ultimately drives the demography of objects over a large range of mass and dimensions in any given volume of arbitrary size of the Universe. In other words, the real MRR is given by the convolution of the MRR of each component with the underlying cosmological scenario that determines the mass interval spanned by galaxies at each redshift and the relative percentage of galaxies of a certain mass with respect to the others (otherwise known as halo mass function).

4.2. The MRR from DM Halo Growth Function $n(M_D, z)$

The similarity of the MRR passing from star clusters to single galaxies of different mass and morphological type and eventually to galaxy clusters suggests that a deep relation exists between the way all these objects populate the MR-plane and the cosmological growth of DM halos.

The distribution of the DM halo masses and their relative number density as a function of the redshift has been the target of numberless studies which culminated with large scale simulations of the structure of the Universe, we quote here one for all, i.e. the Millennium Simulation (Springel et al. 2005). In parallel many studies have investigated the so-called *halo growth function*, HGF as the integral of the *halo mass function*, HMF. Among others (see for instance Angulo et al. 2012; Behroozi et al. 2013) we recall and make use of the results by Lukić et al. (2007) who, using the Λ -CDM cosmological scenario and the HMF of Warren et al. (2006), derive the HGF $n(M_{DM}, z)$. This gives the number density of halos of different masses per $(\text{Mpc}/h)^3$ resulting by all creation/destruction events. The growth function is expressed in terms of the normalized Hubble constant $h = H_0/100$, where H_0 is assumed to be $H_0=70.1$ Km/s/Mpc. The explored interval of redshift goes from 0 to 20. The $n(M_{DM}, z)$ function of Lukić et al. (2007) is shown in Fig. 7⁴. Similar HGF are by Angulo et al. (2012) Behroozi et al. (2013). For more details, see Chiosi et al. (2012).

The analytical representation of the $n(M_D, z)$ function displayed in Fig. 7 is given by

$$n(M_D, z) = \sum_{n=0}^4 A_n(M_D) \times z^n. \quad (11)$$

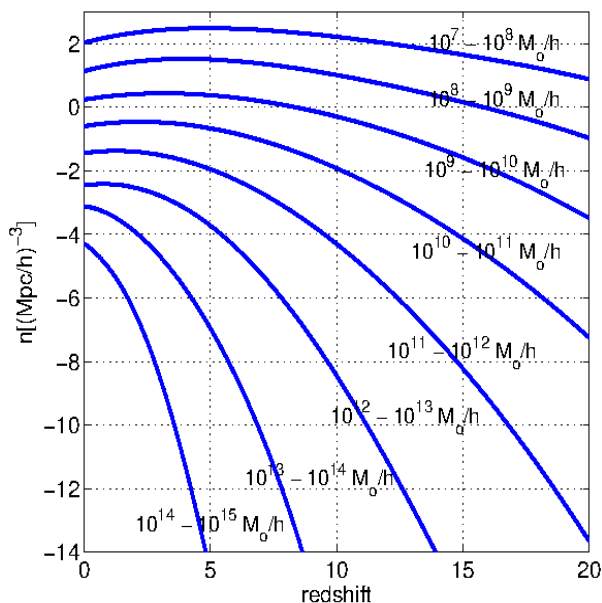
where the coefficients $A_n(M_D)$ are listed in Table 4.1. Then we count the total number of halos per mass-bin $\Delta \log M_D$ at redshift $z = 0$. This is simply given by reading off the values of the curves along the y-axis and interpolating for intermediate values. These are the halos that would nowadays populate the synthetic MR-plane and that should be compared with the observed galaxies. Since the total number of halos read off the Lukić et al. (2007) plot refers to a volume of $1 (\text{Mpc}/h)^3$, any meaningful comparison with observational data requires a suitable scaling of the theoretical values by a suitable factor to match the real volume of the observed portion of the sky from which the data are obtained (see below).

Although what we are going to say is well known, see the pioneer study of Press & Schechter (1974) and Lukić et al. (2007, for ample referencing), for the sake of clarity and as relevant to our discussion we note the following: (i) for each halo mass (or mass interval) the number density is small at high redshift, increases to high values toward the present, and depending on the halo mass either gets a maximum value at a certain redshift followed by a decrease (typical of low mass halos) or it keeps increasing as in the case of high mass halos. In other words, first creation of halos of a given mass (by spontaneous growth of perturbation to the collapse regime) overwhelms their destruction (by mergers), whereas the opposite occurs for low mass halos past a certain value of the redshift; (ii) at any redshift high mass halos are orders of magnitude less frequent than the low mass ones; (iii) at any redshift, the mass distribution of halos has a typical interval of existence whose upper mass end (cut-off mass) increases at decreasing redshift.

⁴ This has been derived from an analytical interpolation of the data presented in Fig. 1 of Lukić et al. (2007).

Table 5. Coefficients of the polynomial interpolation of the relation (11), which provides the number density of haloes $n(M_{DM}, z)$ per $(\text{Mpc}/h)^3$.

Mass [M_\odot/h]	A_4	A_3	A_2	A_1	A_0
5e7	-2.34275e-5	1.28686e-3	-2.97961e-2	2.11295e-1	2.02908
5e8	-2.76999e-5	1.49291e-3	-3.47013e-2	2.13274e-1	1.13553
5e9	-1.31118e-5	6.50876e-4	-2.36972e-2	1.31993e-1	0.23807
5e10	-1.18729e-5	6.65488e-4	-3.17079e-2	1.30360e-1	-0.59744
5e11	-1.47246e-5	8.10097e-4	-4.65279e-2	1.13790e-1	-1.44571
5e12	6.59657e-5	-7.19134e-4	-6.99445e-2	1.06782e-1	-2.45684
5e13	-7.34568e-4	9.99022e-3	-1.65888e-1	-9.48292e-2	-3.11701
5e14	4.89975e-3	-5.17004e-2	-1.61508e-1	-5.83065e-1	-4.28270

**Fig. 7.** The growth function of halos $n(M_D, z)$ reproduced from Lukić et al. (2007).

Given a certain number density of halos N_s , on the $n(M_D, z)$ – z plane of Fig. 7 this would correspond to an horizontal line intersecting the curves for the various masses at different redshifts, i.e. obeying the equation $n(M_{DM}, z) = N_s$. Each intersection provides a pair (M_{DM}, z) which gives the mass of the halos fulfilling the condition $N_s = n(M_D, z)$ at the corresponding redshift z (or vice-versa the redshift satisfying the condition for each halo mass). For any value N_s we get an array of pairs (M_D, z) that can be extrapolated to a continuous function that, with the aid of the Fan et al. (2010) relationship (in which the parameters m and f_σ are fixed), provides the corresponding relationship between the mass in stars and the half-mass radius of the baryonic galaxy associated to a generic host halo to be plotted on the MR-plane.

Repeating the procedure for different values of N_s , we get a manifold of curves on the MR-plane. It turns out that with the N_s corresponding to 10^{-2} halos per $(\text{Mpc}/h)^3$ (that roughly corresponds to the volume surveyed by the SDSS), the curve is just at the edge of the observed distribution of ETGs on the MR-plane. Higher values of N_s would shift it to larger halos (baryonic galaxies), the opposite for lower values of N_s . Why is $N_s = 10^{-2}$ halos per $(\text{Mpc}/h)^3$ so special? Basing on crude, simple-minded arguments we recall that the total number of galaxies observed by the SDSS amounts to about $\approx 10^6$, whereas the volume of Universe covered by it is about $\approx 1/4$ of the whole sky times a depth of $\approx 1.5 \times 10^9$ light years, i.e. $\approx 10^8 \text{ Mpc}^3$, to which the

number density of about 10^{-2} halos per $(\text{Mpc}/h)^3$ would correspond⁵.

The equation $n(M_{DM}, z) = N_s$ with $N_s = 10^{-2}$ or equivalently 10^6 halos per 10^8 Mpc^3 recast to derive the halo mass M_{DM} as a function of z becomes

$$\log M_D = 0.0031546 z^3 - 0.006455 z^2 - 0.183 z + 13.287 \quad (12)$$

from which we get M_D . With the aid of eq.(A.5) we derive the quantity m and from its definition we obtain $M_s = M_D/m$. Finally, from eq. (10) we derive the associated radius R_s .

The analytical fit of the MR relation determined in this way and limited to the mass interval $9.5 \leq \log M_s \leq 12.5$ (M_s in solar units) is

$$\log R_s = 0.048562(\log M_s)^3 - 1.4329(\log M_s)^2 + 14.544(\log M_s) - 50.898. \quad (13)$$

This relation is meant to fit the distribution of the sole ETGs on the MR-plane. We note that the slope gradually changes from 0.5 to 1 and above as we move from the low mass to the high mass range. It is worth recalling here that a similar trend for the slope is also indicated by the observational data (see van Dokkum et al. 2010, and references therein). Owing to the many uncertainties we do not try to formally fit the median of the empirical MRR, but we limit ourselves to show that the locus predicted by $N_s = 10^{-2}$ halos per $(\text{Mpc}/h)^3$ falls on the MR-plane close to the observational MRR. Lower or higher values of the halo number density would predict loci in the MR-plane too far from the observational MRR.

Finally, we call attention on the fact that the locus on the MR-plane defined by the relation (13) is ultimately related to the top end of the mass scale of halos (and their associated baryonic objects) that can exist at each redshift. In other words, recalling that the mass of any intersection pair for $N_s = 10^{-2}$ corresponds to halos becoming statistically significant in number on the observed spatial scale at the associated redshift, this can be interpreted as the so-called cut-off mass in the Press & Schechter (1974) or equivalent formalisms (see Lukić et al. 2007, for details and references). Therefore, this provides also an upper boundary to the mass of galaxies that are allowed to be in place (to collapse) at each redshift. We name these locus the *Cosmic Galaxy Shepherd* (hereafter CGS). All this is shown in Fig. 8, where we also plot the curves relative to $N_s = 10^{-8}$ halos per

⁵ We are well aware that this is a very crude estimate not taking into account many selection effects both in the observations and in the halo statistics based on NB simulations, such as the Lukić et al. (2007) plane itself. However, just for the sake of argument, we can consider it as a good estimate to start with.

$(\text{Mpc}/h)^3$, corresponding to 1 halo per $10^8 (\text{Mpc}/h)^3$, for the sake of comparison.

There are two points to be clarified. First, this way of proceeding implies that *each halo hosts one and only one galaxy and that this galaxy is an early type object matching the selection criteria of the Bernardi et al. (2010) sample*. In reality ETGs are often seen in clusters and/or groups of galaxies and many large spirals are present. Only a fraction of the total population are ETGs. One could try to correct for this issue by introducing some empirical statistics about the percentage of ETGs among all types of galaxy. Despite these considerations, to keep the problem simple we ignore all this and stand on the minimal assumption that each DM halo hosts at least one baryonic component made of stars. This is a strong assumption, on which we will come back again later on. Second, we have assumed that m varies with the halo mass. According to Fan et al. (2010), the empirical estimate of M_{DM}/M_s ratio is about 20-40, our estimate yield a mean value $\langle m \rangle \simeq 20$. However, a slightly higher value for m does not invalidate our analysis, because it would simply shift the location of the baryonic component on the MR-plane corresponding to a given value of N_s . Finally, $f_\sigma = 1$ is a conservative choice. The same considerations made for m apply also to this parameter.

Along the line for the Cosmic Galaxy Shepherd, redshift and cut-off mass go in inverse order, i.e. low masses (and hence small radii) at high redshift and vice-versa. This means that a manifold of MRRs defined by eqn. (10), each of which referring to a different collapse redshift, can be selected, and along each MRR only masses (both parent M_{DM} and daughter M_s) smaller than the top end are permitted, however each of which with a different occurrence probability: low mass halos are always more common than the high mass ones. In the observational data, it looks as if ETGs should occur only towards the high mass end of each MRR, i.e. along the locus on the MR-plane whose right hand side is limited by the CGS. This could be the result of selection effects, i.e. (i) galaxies appear as ETGs only in a certain interval of mass and dimension and outside this interval they appear as objects of different type (spirals, irregulars, dwarfs etc.), or (ii) they cannot even form or be detected (e.g. very extended objects of moderate/low mass). Finally, in addition to this, we argue that another physical reason limits the domain of galaxy occurrence also on the side of the low mass, small dimension objects. We will come to this later on.

4.3. More on the cosmic galaxy shepherd

If we compare the present-day position of the reference hydrodynamical models on the MR-plane with the region populated by real galaxies (see Fig. 5 and/or Fig. 6), at a first glance one would be tempted to conclude that only the high mass models suited to massive ETGs fairly agree with observations, whereas the low mass ones (and to some extent also those of intermediate mass) apparently have too large radii with respect to their masses. However, before drawing the conclusion that essentially the models fail to reproduce the data, it is worth recalling that the observational distribution of galaxies on the MR-plane result from the combined action of many factors not yet taken into account by our analysis. Is the observational sequence of ETGs populated only by galaxies behaving as our massive ones? Or what else? Since for any value of the halo mass there is a certain redshift below which halos of this mass start decreasing in number by mergers (Lukić et al. 2007), galaxies generated by those halos become more and more unlikely as it should be the case for our low mass models. Indeed when at a given redshift we have

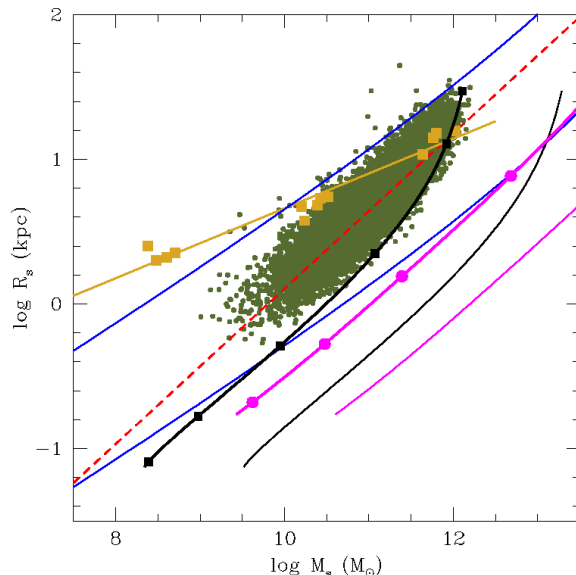


Fig. 8. The *Cosmic Galaxy Shepherd* (CGS) and the corresponding locus of DM parent halos (the black solid thick and thin lines, respectively) for the number density of $N_s = 10^{-2}$ halos per $(\text{Mpc}/h)^3$. In addition to this we show the case with $N_s = 10^{-8}$ halos per $(\text{Mpc}/h)^3$ (the magenta solid thick and thin lines). The various loci are plotted onto the observational MR-plane (see text for all details). We also draw the observational data for the HB sample of Bernardi et al. (2010) with their linear fit, and two theoretical MRR from eqn. (10) by Fan et al. (2010) (solid thin blue lines), relative to $z = 0$ and $z = 10$, with $m = 15$ and $f_\sigma = 1$. In addition to this, the present day position of the reference galaxy models and their linear fit are shown (the golden filled squares and solid line). Finally, the filled black squares and magenta circles show the CGS at different values of the redshift ($z=0, 1, 5, 10, 15$, and 20) for the two cases of the number density per $(\text{Mpc}/h)^3$.

assumed the existence of halos of any mass, we have neglected this important effect. Therefore, the situation may occur that halos/baryonic model galaxies are calculated and plotted onto the MR-plane even though according to the above arguments their existence is very unlikely.

On this ground, we argue that the observational MRR of ETGs (galaxies in general) is the result of convolving two agents: the halo growth function providing the number density of halos of different mass as a function of the redshift (in the concordance Λ -CDM Universe), and the fundamental MRR determining the probable size of a galaxy as a function of its mass and formation redshift after the collapse.

5. Tightening things up in cosmological context

In this section we seek a common explanation for the observational distribution of astronomical objects going from GCs, to galaxies like DGs, ETGs (and to a less extent also Spiral Galaxies) to Clusters of Galaxies, the mass of which spans about eleven orders of magnitude. The situation is shown in Fig. 9. The pale-blue filled circles are the normal/giant ETGs, the DGs, the GCs, and the GCGs. No distinction is made among different groups or sources of data. The aim here is to qualitatively display the region of the MR-plane populated by real objects of different mass, size and morphological type.

Let us quickly summarize once more the main features of the distribution:

(i) The family of GClS is well detached from the body of normal/giant ETGs (let us say those with mass larger than about $10^{10} M_{\odot}$). However, the region in between is populated by DGs. At the top of the distribution there are the GCGs with the largest radii and masses. The richest sample to our disposal is made of ETGs (the Spiral Galaxies occupy more or less the same region). The relative number of objects per group is not indicative of the real number frequencies because severe selection effects are present. The best fit of the ETGs data from the various sources yields the relations of eqn.(1) for Burstein et al. (1997), eqn.(2) for Bernardi et al. (2010) and eqn.(3) for the WINGS data, in which only objects with $M_s \geq 10^{10} M_{\odot}$ are considered not to contaminate the samples with DGs. Since the slopes differ by 0.1 and the zero-points by 0.88, we consider the three relationships fully equivalent.

(ii) If we extrapolate any of the relation above holding for massive ETGs downward to the mass range of GCs and upward to that of GCGs, we see that the same relation provides a lower limit to GClS, passes through ω Cen and M32, provides the lowest limit to the distribution of DGs, and finally hit the region of GCGs.

(iii) There are no galaxies in the semi-plane for radii R_s smaller than the values fixed by relation (2), independently of the galaxy mass, but for the so-called “compact galaxies” that we will examine in a forthcoming paper (Chiosi et al. 2020 in preparation).

(iv) Starting from the cosmological HMF we have been able to derive a MRR, named Cosmic Galaxy Shepherd, providing a sort of mass limit in the MR-plane to the distribution of ETGs. The analytical expression for this limit is given by eq.(13) and it plays the same role as the three MRR above. The only difference is that it gradually changes its slope from ≈ 0.5 to ≈ 1 at increasing the galaxy mass. Extending the Cosmic Galaxy Shepherd down to GCs and up to GCGs a different analytical approximation is possible

$$\log R_s = 0.007584(\log M_s)^3 - 0.1874(\log M_s)^2 + 1.908(\log M_s) - 9.027 \quad (14)$$

with R_s and M_s in the usual units. This line is the analog of the linear global fit above. As already said it represents the cut-off mass of the halo distribution function at varying redshift however translated onto the R_s vs M_s plane. This coincidence provides a profound physical meaning to the transverse line splitting the MR-plane in two regions, i.e. the region in which the vast majority of galaxies are found and the region of avoidance.

(v) Galaxy models tell a more complicated situation. The monolithic hydrodynamical models by Chiosi & Carraro (2002) and the series of early-hierarchical models by Merlin et al. (2012, shortly indicated Mod-M) yield the following MRRs

$$\log R_s = 0.331 \log M_s - 3.644 \quad \text{Mod - A} \quad (15)$$

$$\log R_s = 0.273 \log M_s - 1.994 \quad \text{Mod - B} \quad (16)$$

$$\log R_s = 0.241 \log M_s - 1.750 \quad \text{Mod - M} \quad (17)$$

It is worth noting that both the slope and zero point of models Mod-A and Mod-B change with the redshift, models Mod-M are similar to models Mod-B, and finally the variation in slope is smaller than that in zero-point. Recalling that the three groups of models are calculated with different redshift of galaxy formation (hence initial density) but similar internal physical processes, this means that the slope is fixed by the physical structure

of the models, whereas the zero-point is reminiscent of the initial density. The slope of the above relations is not identical to that of ETGs, relation (2), but more similar to that of DGs. However, along the sequence of each group, the most massive models in which star formation is terminated fall into the region of ETGs.

The Illustris models yield similar relationships, once they are split in two groups

$$\log R_s = 0.297 \log M_s - 2.513 \quad \text{for } \log M_s \leq 10.5 \quad (18)$$

and

$$\log R_s = 0.519 \log M_s - 4.492 \quad \text{for } \log M_s \geq 10.5 \quad (19)$$

The first relation holds for the vast majority of models and reminds the one of normal DGs, whereas the second relation holds for a small group of objects and is close to the case of ETGs. Furthermore, the models of the first group with the MRR of eq. (18) are the seeds of bigger galaxies, which after reaching a suitable value by mergers and terminating all star formation activity, give origin to galaxies located along the MRR of eq (19).

Finally, the MRR of eq.(10) of Fan et al. (2010) with slope 0.333 is nearly identical to that of theoretical models, i.e. eqns. (15), (16), (17), and (18). In other words, by construction the Fan et al. (2010) lines visualize galaxies born at the same redshift but with different masses. The most important issue here is “Why observational MRRs for ETGs are so different from the theoretical ones but for the most massive objects?”

(vi) To answer the above question, we start from the following general considerations. It goes without saying that the gravitational collapse of proto-clouds giving origin to a galaxy is in general accompanied by important side phenomena such as star formation and consequent energy feed-back, gas cooling and heating, galactic winds removing energy and mass, mass and energy acquisition by mergers, etc. Therefore the theoretical models may change depending on the detailed physical description of all these energy producing/removing phenomena together with those for the mass acquisition/loss. In this scenario, the ideal reference galaxy formation model would be the dissipation-less collapse of DM+BM halos originated from primordial density perturbations of rms amplitude toward the equilibrium structure (Gott & Rees 1975; Faber 1984; Burstein et al. 1997). In brief, if δ is the rms amplitude of primordial density perturbations of total mass $M_T = M_{DM} + M_{BM}$

$$\delta \propto M_T^{-\frac{1}{2} - \frac{n}{6}} \quad (20)$$

where M_T is the mass at the initial red-shift, and n is the slope of the density fluctuation δ . After collapse, the equilibrium structure of a halo originated from given δ and M_T follows the relations (Gott & Rees 1975)

$$R_T \propto \delta^{-1} M_T^{\frac{1}{3}} \quad (21)$$

from which we immediately get

$$R_T \propto M_T^{\frac{5+n}{6}} \quad (22)$$

Inserting $n = -1.8$, the power spectrum of CDM (Blumenthal et al. 1984), we get the relation

$$R_T \propto M_T^{0.53} \quad (23)$$

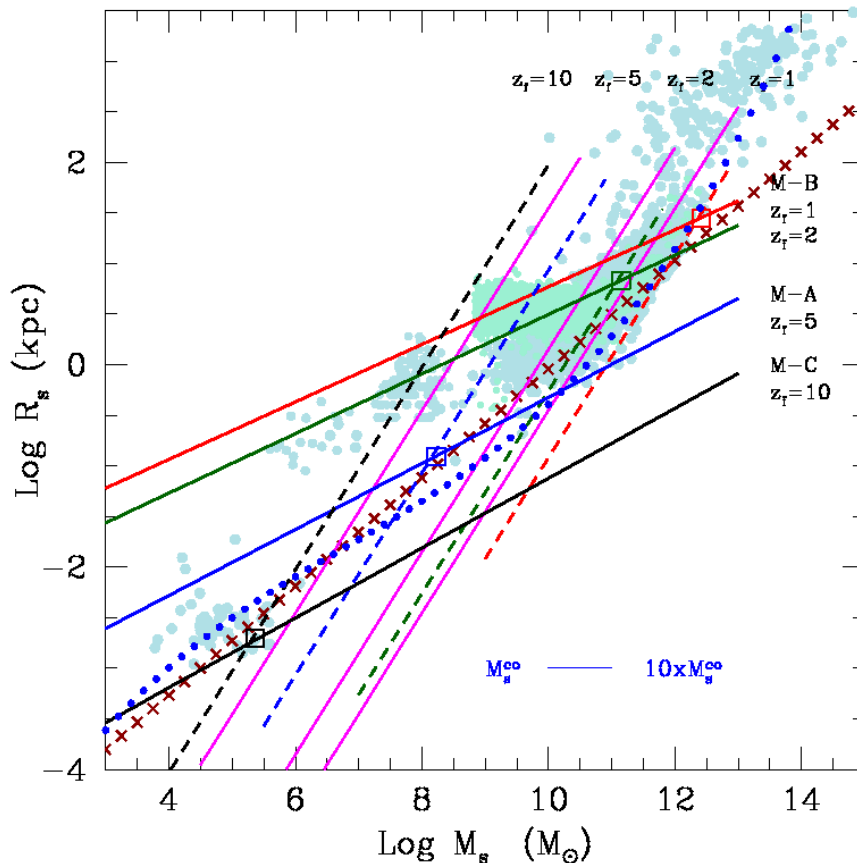


Fig. 9. The Mass-Radius Relationship: comparison between data and theory. Radii R_s and stellar masses M_s are in kpc and M_\odot , respectively. The pale-blue filled circles are all the data considered in this study, the pale green filled circles the models of Illustris. The dark-red thick crossed line is the linear best fit of normal ETGs ($M_T \geq 10^{10} M_\odot$) given by eq.(2), however prolonged down to the region of globular clusters and upwards to that of galaxy clusters. The four long-short dashed lines labeled Mod-A ($z_f = 5$, blue), Mod-B ($z_f = 1$, red and $z_f = 2$, dark green) and Mod-C ($z_f = 10$ black) are the analytical relationships of eq. (31) showing the loci of galaxy models with different mass but constant initial density for different values of redshift of galaxy formation z_f as indicated. These lines are the best fit of the the models by Chiosi & Carraro (2002), Merlin et al. (2012) and Chiosi et al. (2012), see Tables B.1, B.2, and B.3. The magenta solid lines are the MRRs of galaxies in virial conditions and with different velocity dispersion (50, 250 500 km/s from left to right) The dashed black lines labeled by different values of z_f are the MRRs expected for galaxies with total mass equal to $50 \times M^{CO}(z)$, the cut-off mass of the Press-Schechter at varying z_f according to relation (32). These lines go in pairs with the best-fit lines of models of identical initial density labeled by the same color. The large empty squares visualize the intersections between the lines of constant initial density and the MRRs for $50 \times M^{CO}$ galaxies for equal values of the redshift. All the intersections lie very close to the relation of eq.(2) shown by the dark-red crossed line. This is the linear interpretation of the observed MRR, i.e. the analytical demonstration of Section 5. Finally, the curved blue dotted line shows the expect MRR from the cosmological distribution of DM halos and stellar contents in turn of different mass by Lukić et al. (2007), however extended to the domain of globular clusters and galaxy clusters (see the text for more details). Note the ever changing slope decreasing with the halo mass and the stellar mass turn in. Remarkably the curved line first runs very close to the large empty squares, second to linear fit of the data (crossed line), and third accounts for the observed MRR passing from globular clusters to galaxy clusters (about ten orders of magnitude difference in the stellar mass). Finally, the horizontal blue line shows the interval for M_s corresponding to initial masses $M^{CO}(z) < M_T < 10 \times M^{CO}(z)$ (the percentage of galaxies in this interval amounts to $\approx 15\%$) highlights that at each redshift the high-mass edge of the MRR is not a sharp border.

The slope of the MRR derived from the dissipation-less collapse is about same of eqn. (2) for ETGs, whereas the proportionality constant cannot be fixed by these simple arguments. For the sake of a simple discussion, we approximate $M_T \simeq M_D$ and $R_T \simeq R_D$ and replace eqn. 23 with

$$R_D \propto M_D^{0.53} \quad (24)$$

Inside this halo up a galaxy made of stars is built up over years with mass M_s and half-mass radius R_s . Using the Illustris models (see Sect. 3) we may derive the relationships $\log R_s =$

$\gamma \log R_D + \eta$ and $\log M_s = \alpha \log M_D + \beta$. Inserting these relations into eqn.(24) we obtain

$$\log R_s = 0.53 \frac{\gamma}{\alpha} \log M_s - 0.53 \frac{\gamma\beta}{\alpha} - \eta + k\gamma \quad (25)$$

where the constant k owes its origin to the initial indeterminacy of the proportionality factor in eqn. (24). Limiting to models at $z = 0$ and to the region of the MR-plane in which the MRR is evident (roughly for $\log M_s \geq 10.5$) we get $\alpha = 0.533$, $\beta = 4.607$, $\gamma = 0.544$, and $\eta = -0.103$, whereas for smaller masses ($\log M_s < 10.5$ we obtain $\alpha = 0.883$, $\beta = 0.088$, $\gamma = 0.171$, and

$\eta = 0.377$. With these values we have

$$\log R_s = 0.541 \log M_s - 4.702 + k\gamma \quad \text{for } \log M_s > 10.5 \quad (26)$$

$$\log R_s = 0.102 \log M_s - 0.017 + k\gamma \quad \text{for } \log M_s < 10.5 \quad (27)$$

The term $k\gamma$ cannot be determined unless the constant k is specified by fixing the initial conditions of the collapsing proto-halo. The slope of relation (26) does not significantly differ from the one of eqn. (23) dissipation-less collapse, and eqn. (2), the empirical MRR of Bernardi et al. (2010). This is possible only for the most massive galaxies of M-MRR manifold. For galaxies of smaller mass the final relation, eqn. (27), largely departs from it.

Based on the above considerations, one might be tempted to conclude that equation (2) represents the locus in the MR-plane of galaxies whose formation closely follows the dissipation-less collapse from the initial state (mass, radius, mean density, etc.) to the final one indicated on the MR-plane by the final values of M_s and R_s . Were this the case, special conditions ought to hold for all objects like the DGs that clearly deviate from this relationship. The explanation is different for the monolithic and hierarchical scenario:

a) In the standard monolithic view, in addition to star formation and the various gas heating and cooling processes, galactic winds are another key ingredient to consider. The analysis made by Chiosi & Carraro (2002) is particularly useful. Following their reasoning, we derive the relationship between the gas mass lost in the wind as function of the mass in stars in the galaxy models, the low mass ones in particular because the DGs galaxies show the largest deviation from the observed MRR, eq. (2) or eq. (23). Using the entries of Table B.1 in Appendix B (those for Mod-B), we obtain the following relations

$$\log\left(\frac{R_s}{R_s^0}\right) = -0.264 \log M_s + 3.271 \quad (28)$$

$$\log\left(\frac{M_{g,w}}{M_{g,i}}\right) = -4.038 \log M_s + 5.490 \quad (29)$$

$$\log\left(\frac{R_s}{R_s^0}\right) = 1.065 \log\left(\frac{M_{g,w}}{M_{g,i}}\right) + 1.825 \quad (30)$$

where R_s is the current effective radius of the galaxy, R_s^0 the radius it would have if strictly following eq. (2), and $M_{g,w}/M_{g,i}$ the gas mass lost in the galactic wind normalized to the initial gas mass. The last relation shows that $\log(R_s/R_s^0)$ increases with $M_{g,w}/M_{g,i}$. The stronger the galactic wind, the larger is the final effective radius. In other words, galaxies tend to depart from the locus represented by eq. (2) and/or eq.(23) at increasing mass and galactic winds in turn, the low mass ones having the strongest effect. In addition to this, we noted that the relative efficiency of galactic winds tends to decrease at increasing initial density of the proto-galaxy (compare models A and B in Table B.1 of the Appendix B). This means that the effect of galactic winds in inflating low mass galaxies of high initial density is lower so that their final radius will be closer to the value predicted by eqs. (2) and/or (23). *The conclusion is that the flatter slope of the theoretical MRR in the monolithic scheme is likely caused by galactic winds.*

b) In the case of the hierarchical scenario, the situation is more complicated because mergers and galactic winds both concur to inflate a galaxy. To clarify the issue Chiosi & Carraro (2002) discussed the case of a merger between two galaxies calculated by Buonomo (2000) of which they knew all details: a $2 \times 10^{11} M_\odot$ galaxy was simulated by merging two disc-like subunits, each one with total mass (BM+DM) equal to $1 \times 10^{11} M_\odot$,

and ratio of BM to DM equal to 0.1. At the time of encounter the mass in stars of each sub-unit was about $M_s = 6 \times 10^8 M_\odot$ and the mass in gas $M_g = 9.3 \times 10^9 M_\odot$. The merger was accompanied by little star formation, so that the total mass in stars, gas, and BM of the newly formed galaxy was $M_s = 1.2 \times 10^9 M_\odot$, $M_g = 1.8 \times 10^{10} M_\odot$ and $2 \times 10^{10} M_\odot$, respectively. The effective radius of the composite object was $R_s = 8.4$ kpc and its shape reminded that of an elliptical one. The merger galaxy was shown in Fig. 5 by the big empty star. It looks like our Mod-B of comparable total star mass except for the fact that it is more diffuse. Basing on these calculations, we estimate that merging two single disc-like objects made of stars and gas to build up a galaxy with twice as much total mass as the component galaxies would generate an elliptical-like galaxy, the star mass and effective radius of which are smaller and higher, respectively, by $\Delta M_s/M_s \simeq -0.9$ and $\Delta R_s/R_s \simeq 0.5$ compared to the case of an elliptical of the same mass but obtained with the monolithic scheme. However, if mergers might inflate the final object (see Hernquist 1992, 1993) and therefore explain the position of DGs (see also the many models of the Illustris database calculated in the hierarchical framework), they can hardly explain the observational MRR of ETGs. In other words, mergers may concur to build up a galaxy, but are not determining the final MRR.

On consideration of these premises, we suggest that the observational MRR of ETGs, either eqn.(1) or eqn.(2) or eqn.(3), represents the locus on the MR-plane of galaxies whose present-day structure closely mimics the ideal situation of mechanical (virial) equilibrium and passive evolution. Their MRR is also the boundary between permitted and forbidden regions of the MR-plane. The DGs or less massive objects have a different interpretation, because they significantly depart from the above evolutionary scheme and the MRR holding for ETGs.

(vii) To prove the above statement we strictly follow the method proposed long ago by Chiosi & Carraro (2002) however updated to the recent theoretical and observational data. To this aim, we draw on Fig.9 two loci and a mass interval as function of the initial density (redshift):

(a) The first locus is the present-day MRR traced by model galaxies of different mass but similar initial density at varying redshift. Most of this issue has already been examined in detail but from a different perspective in Sect.3.4. The novelty here is to provide an easy to use relationship yielding the expected MRR of theoretical models as a function of the formation redshift z_f for the bulk of the stellar content of a galaxy. Using all the models to our disposal, i.e. Chiosi & Carraro (2002) and Merlin & Chiosi (2006, 2007); Merlin et al. (2010, 2012); Chiosi et al. (2012) we get the relation

$$\log R_s = [-1.172 - 0.412(1 + z_f)] + [0.244 + 0.0145(1 + z_f)] \log M_s \quad (31)$$

The following cases are shown in Fig. 9: $z_f \simeq 1$, $z_f \simeq 2$, $z \simeq 5$ and $z_f \simeq 10$. The procedure is safe thanks to the regular behavior of the models and the density-mass relationship of eq. (23). This relationship is compatible with the MRRs predicted by Fan et al. (2010), see eq.(10). Finally, they also agree with the theoretical models of Illustris by Vogelsberger et al. (2014a,b).

(b) The second locus is the MRR for galaxies with the statistical maximum mass allowed by the underlying HGM at any redshift. This relationship can be derived (either graphically or numerically) from any HGM in literature e.g. Lukić et al. (2007), or Angulo et al. (2012), or Behroozi et al. (2013). In Sect. 4.2 we have derived this relation for the HGF of Lukić et al. (2007): see the analytical expression of eq.(13) or its extension to the

whole MR-plane given by eq. (14). However, for the sake of a very simple yet instructive analytical approach we prefer to make use here of the classical Press & Schechter (1974) function of haloes as a sort of mass distribution function for galaxies: in the simplistic assumption of one galaxy per halo it provides the relative number of galaxies per mass bin at varying redshift. Furthermore, we consider the cut-off mass M_T^{CO} of the Press & Schechter (1974) function as the maximum mass limit of the galaxy masses at the current value of the redshift. According to the Press & Schechter (1974) formalism, varies with the redshift according to

$$M_T^{CO} = M_N \times (1+z)^{-\frac{6}{n+3}} \quad (32)$$

The exponent n is the slope of the initial power spectrum of the perturbations, M_N is a suitable normalization mass scale. At any redshift, most of the galaxies have total masses smaller than M_T^{CO} , even if higher values cannot be excluded. Indeed, the fractional mass in (or fractional number of) galaxies with mass greater than M_T^{CO} is a function of n . For $n=-1.8$, the percentage of galaxies in the mass interval $M_T^{CO} < M_T < 10 \times M_T^{CO}$ amounts to about 15% and in the range $10 \times M_T^{CO} < M_T < 100 \times M_T^{CO}$ to about 1%. Therefore, at any redshift galaxy masses up to say $10 \times M_T^{CO}$ may occur with a sizable probability.

With the aid of the relationships presented in Tables B.1, B.2, and B.3 of Appendix B (providing the mass in stars and effective radius of BM as a function of M_T) and limited to the case with $M_T = \gamma M_T^{CO}$ for $\gamma = 10$ and power spectrum $n = -1.8$, we get

$$R_s = 16.9 \times 10^{12} \times \gamma^{-0.79} \times (1+z)^{3.96} \times M_s \quad (33)$$

where R_s and M_s are in kpc and M_\odot . These loci are shown in Fig. 9 by the dotted lines labeled by the redshift, namely $z \approx 1$, ≈ 2 , ≈ 5 and ≈ 10 . *On the MR-plane, they represent the right-most extension of the lines of constant density and maximum galaxy mass in turn. At decreasing redshift the boundary progressively moves toward higher masses.* Similar lines and conclusions can be recovered using the HGF of Lukić et al. (2007) or Angulo et al. (2012), or Behroozi et al. (2013).

(c) Finally, the third locus is the expected interval for M_s (the present day star mass in a galaxy) for objects with total mass comprised between M_T^{CO} and $10 \times M_T^{CO}$ as a function of the redshift. To this aim, the relation $M_s(M_T)$ has been plugged into relation (32) for M_T^{CO} . The permitted intervals are shown in Fig. 9 by the horizontal lines labeled M_s^{CO} . The interval for M_s going from $10^{10} M_\odot$ to $10^{12} M_\odot$ is fully compatible with a redshift interval for the formation of the majority of stars in a galaxy from 2 to 1. This interval is also the mass range over which at each redshift the probability for the occurrence of massive galaxies falls to negligible values. In other words, on the MR-plane the right-hand border of the MRR has a natural width.

(viii) Having set the whole scene, we proceed to the final step. If our reasoning is correct the basic relationship for ETGs, either eqs. (2) or (23), however extended to the whole mass range of the objects under consideration (from GCs to GCGs) should correspond to the intersection of lines of constant initial density and the lines $\gamma M_T = M_T^{CO}(z)$ for equal values of the redshift, at least for all values of redshift greater than about 1. This indeed is what we see in Fig. 9 (the large empty squares). This result provides the analytical demonstration that the observational MRR stems from the product of two main agents: the mechanism governing galaxy formation and evolution (monolithic, early-hierarchical, or fully hierarchical) and the HGF and

its variations with the redshift. It follows from this analysis that the MRR is the locus of objects in mechanical (virial) equilibrium and passive or nearly passive evolutionary stage. This MRR is mainly traced by ETGs, GCs, a few DGs and GCGs. The large majority of DGs lie above it. We have already argued about the physical reasons why DGs (but for few exceptions) cannot yet lie on this MRR. Ongoing active star formation and strong galactic winds. This finding confirms the result obtained by D’Onofrio et al. (2019b): only passive galaxies (strongly decreasing their luminosity as the redshift goes to zero) trace the MRR on the MR-plane with a slope 0.5 to 1, the highest value being reached by objects that suffered the strongest luminosity decrease with the redshift, i.e. those that long ago ceased their stellar activity, likely the massive ones. Spiral galaxies occupy nearly the same location on the MR-plane thus suggesting that their ongoing star formation is not affecting the overall situation of mechanical equilibrium of the whole system. Given that linear relations have been used (in compliance with the *euclidean “ruler and compass” method*), the result is a straight line visualized by the large empty squares. The correct evaluation would be given by numerically folding the adopted HGF, Lukić et al. (2007) in our case, with the loci on the MR-plane populated at the present time by galaxies of different mass but the same initial density born at different redshifts. The result is the crossed dark-red line shown in Fig. 9, i.e. eqs. (13) and/or (14).

(ix) Finally, it is worth noting that the slope of MRR derived from the HGF is about 1 in the range of massive galaxies (say above $10^{12} M_\odot$), i.e. formally identical to the MRR that one would derive from the virial theorem. This coincidence might suggest that the observed MRR and its slope are driven by the virial condition whereas the true driver of the MRR slope is the HGF, more precisely its fall off toward high values of the halos’ masses at any value of the redshift. On the other hand, all objects along the MRR are indeed in virial conditions once any mechanical process and star formation are at rest.

6. General remarks and conclusions

What can we learn from all these observational hints, and striking coincidence between data and theory? Seeking for a coherent picture, one is tempted to suggest the following scenario:

(i) According to their initial density galaxies of given total mass will distribute in the MR plane along lines of type A and/or B and/or C. The initial density is not constant, but decreases as z_f tends to zero. The permitted mass intervals for the total (and baryonic) mass of the galaxies is not constant, but increases at decreasing redshift. At redshifts of about 1 to 2, galaxies with total mass up to a few $10^{12} M_\odot$ are in place and their MRR will extend up to the range populated by the galaxies we see today.

(ii) The expectation is that galaxies of any mass and initial density crowd a strip bounded by the lines of maximum and minimum initial density (say redshifts from about 10 to 1–2) and the line corresponding to their maximum mass in the HGF for the same redshifts.

(iii) In this context, the semi-plane below either relation (23) in the simple description or relation (14) based on the Cosmic Galaxy Shepherd and the HGF in turn, is void of galaxies, because they would be too massive at given initial density (redshift) to be compatible with the maximum mass of the HGF in general for all values of the redshift.

(iv) In the semi-plane above relation (23) and/or (14), the available data are not statistically complete, so that in the range of low mass galaxies we have only those of the Local Group

(M32 and ω Cen include). Dwarf galaxies of large effective radius are simply not in the sample. Observations of the Fornax cluster (Im et al. 2001) have revealed a new type of DGs. They have intrinsic sizes of about 100 pc and are more compact and less luminous than other known compact dwarf galaxies, yet much brighter than globular clusters. Their absolute magnitude is about $M_B = -13$ (two magnitudes fainter than M32). Are these objects representing the low mass tail of galaxies falling along line A in Fig. 9? More observational data may clarify this issue.

(vi) GCs are more difficult to discuss because, being those we have considered bound to the Milky Way, they have certainly suffered many external (and internal) dynamical processes that may have changed their present mass and radius.

(vii) Finally, there are GCGs to comment. Masses of their bulk stellar content and half-mass radii of the ideal sphere in which stars are contained, are by still highly uncertain so that on the MR-plane they do not trace a sharp MRR but rather a broad region. Part of the scatter is perhaps to GCGs still evolving towards the equilibrium state, part to observational uncertainties. Suffice here that the same theoretical MRR can pass through all the regions of the MR-plane crowded by objects going from GCs to GCGs.

(viii) To conclude, we endeavor to speculate on the origin of the present-day MRRs and their differences passing from GCs to DGs, ETGs and GCGs. The focus goes to DGs and ETGs, however also GCs and GCGs are considered. For all of them, we suggest a common origin stemming from the interplay among several processes, i.e. the initial density together with total mass that drive the star formation history, the efficiency of energy feed-back in triggering galactic winds that affect the mass and the size of the objects, the merger history of a galaxy, and the steady increase of the maximum mass reachable by the HGF at decreasing redshift and or decreasing mean density of the Universe. High density (low mass) objects are the first to form stars in the remote past followed by objects of lower density (higher mass). The MRRs of eq.(2) or (23) simply reflect the above interplay. Galaxies as massive as a typical $10^{12} M_\odot$ object can be in place at redshifts from 2 to 1. After the first initial activity, passive evolution is expected. They generate the MRR of dynamically stable and passively evolving objects in virial conditions, the shape of which is driven by the cosmological distribution (mass and relative number density) of the halos hosting the visible galaxy. Since the HGF is not a linear function, the slope of the MRR continuously varies from ≈ 0.5 to ≈ 1 , Objects in similar physical conditions (passive evolution and virial regime) but with lower mass (say up to $10^{10} M_\odot$), closely follow the MRR of the dissipation-less case (slope of about 0.5 or so) and yet are in virial conditions (see GCs and DGs like M32 and ω Cen). All other galaxies being still far from these ideal conditions because of active star formation, presence of galactic winds, occurrence of repeated mergers, etc., strongly deviate from the ideal MRR of objects in mechanical and thermal equilibrium. The information for GCGs is still in progress so that no firm conclusions can be drawn, even though they seem to fit for this scenario.

Acknowledgements. We like to thank Prof. L. Secco and Dr. R. Caimmi for very useful discussions on many aspects of this study. C.C. thanks the Department of Physics and Astronomy of the Padua University for the hospitality and computational support.

References

Agertz, O. & Kravtsov, A. V. 2016, *ApJ*, 824, 79
 Angulo, R. E., Springel, V., White, S. D. M., et al. 2012, *MNRAS*, 426, 2046
 Behroozi, P. S., Wechsler, R. H., Wu, H.-Y., et al. 2013, *ApJ*, 763, 18

Bernardi, M., Meert, A., Vikram, V., et al. 2014, *MNRAS*, 443, 874
 Bernardi, M., Roche, N., Shankar, F., & Sheth, R. K. 2011, *MNRAS*, 412, L6
 Bernardi, M., Shankar, F., Hyde, J. B., et al. 2010, *MNRAS*, 404, 2087
 Blumenthal, G. R., Faber, S. M., Primack, J. R., & Rees, M. J. 1984, *Nature*, 311, 517
 Bryan, G. L. & Norman, M. L. 1998, *ApJ*, 495, 80
 Buonomo, F. 2000, PhD thesis, Astronomy Department, Padova University, Vicolo Osservatorio 2, 35122 Padova, Italy
 Burstein, D., Bender, R., Faber, S., & Nolthenius, R. 1997, *AJ*, 114, 1365
 Caminha, G. B., Grillo, C., Rosati, P., et al. 2017, *A&A*, 607, A93
 Cariddi, S., D'Onofrio, M., Fasano, G., et al. 2018, *A&A*, 609, A133
 Cava, A., Bettoni, D., Poggianti, B. M., et al. 2009, *A&A*, 495, 707
 Chiosi, C. & Carraro, G. 2002, *MNRAS*, 335, 335
 Chiosi, C., Merlin, E., & Piovan, L. 2012, arXiv e-prints [arXiv:1206.2532]
 Corwin, Jr., H. G., Buta, R. J., & de Vaucouleurs, G. 1994, *AJ*, 108, 2128
 de Vaucouleurs, G., de Vaucouleurs, A., Corwin, Jr., H. G., et al. 1991, Third Reference Catalogue of Bright Galaxies. Volume I: Explanations and references. Volume II: Data for galaxies between 0^h and 12^h . Volume III: Data for galaxies between 12^h and 24^h .
 D'Onofrio, M., Bindoni, D., Fasano, G., et al. 2014, *A&A*, 572, A87
 D'Onofrio, M., Chiosi, C., Sciarra, M., & Marziani, P. 2019a, *ApJ*, submitted
 D'Onofrio, M., Sciarra, M., Cariddi, S., Marziani, P., & Chiosi, C. 2019b, *ApJ*, 875, 103
 Engler, C., Pillepich, A., Joshi, G. D., et al. 2020, arXiv e-prints, arXiv:2002.11119
 Faber, S. M. 1984, in *Large-Scale Structure of the Universe*, ed. G. Setti & L. Van Hove, 187
 Fan, L., Lapi, A., Bressan, A., et al. 2010, *ApJ*, 718, 1460
 Fasano, G., Marmo, C., Varela, J., et al. 2006, *A&A*, 445, 805
 Fasano, G., Vanzella, E., Dressler, A., et al. 2012, *MNRAS*, 420, 926
 Fritz, J., Poggianti, B. M., Bettoni, D., et al. 2007, *A&A*, 470, 137
 Fritz, J., Poggianti, B. M., Cava, A., et al. 2011, *A&A*, 526
 Geha, M., Blanton, M. R., Masjedi, M., & West, A. A. 2006, *ApJ*, 653, 240
 Genel, S., Nelson, D., Pillepich, A., et al. 2018, *MNRAS*, 474, 3976
 Genel, S., Vogelsberger, M., Springel, V., et al. 2014, *MNRAS*, 445, 175
 Girelli, G., Pozzetti, L., Bolzonella, M., et al. 2020, arXiv e-prints, arXiv:2001.02230
 Gott, III, J. R. & Rees, M. J. 1975, *A&A*, 45, 365
 Graham, A. W. 2011, ArXiv e-prints: 1108.0997 [arXiv:1108.0997]
 Graham, A. W. 2013, *Elliptical and Disk Galaxy Structure and Modern Scaling Laws*, ed. T. D. Oswalt & W. C. Keel, 91
 Gullieuszk, M., Poggianti, B., Fasano, G., et al. 2015, *A&A*, 581, A41
 Guo, Y., McIntosh, D. H., Mo, H. J., et al. 2009, *MNRAS*, 398, 1129
 Hamraz, E., Peletier, R. F., Khosroshahi, H. G., et al. 2019, *VizieR Online Data Catalog*, J/A+A/625/A94
 Hernquist, L. 1992, *ApJ*, 400, 460
 Hernquist, L. 1993, *ApJ*, 409, 548
 Hinshaw, G., Larson, D., Komatsu, E., et al. 2013, *ApJS*, 208, 19
 Huang, K.-H., Fall, S. M., Ferguson, H. C., et al. 2017, *ApJ*, 838, 6
 Im, M., Faber, S. M., Gebhardt, K., et al. 2001, *AJ*, 122, 750
 Karim, A., Schinnerer, E., Martínez-Sansigre, A., et al. 2011, *ApJ*, 730, 61
 Kissler-Patig, M., Jordán, A., & Bastian, N. 2006, *A&A*, 448, 1031
 Krumholz, M. R. & Tan, J. C. 2007, *ApJ*, 654, 304
 Kuchner, U., Ziegler, B., Verdugo, M., Bamford, S., & Häußler, B. 2017, *A&A*, 604, A54
 Lada, C. J. & Lada, E. A. 2003, 41, 57
 Lukić, Z., Heitmann, K., Habib, S., Bashinsky, S., & Ricker, P. M. 2007, *ApJ*, 671, 1160
 Mancini, C., Matute, I., Cimatti, A., et al. 2009, *A&A*, 500, 705
 Merlin, E., Buonomo, U., Grassi, T., Piovan, L., & Chiosi, C. 2010, *A&A*, 513, A36
 Merlin, E. & Chiosi, C. 2006, *A&A*, 457, 437
 Merlin, E. & Chiosi, C. 2007, *A&A*, 473, 733
 Merlin, E., Chiosi, C., Piovan, L., et al. 2012, ArXiv e-prints 1204.5118 [arXiv:1204.5118]
 Moretti, A., Gullieuszk, M., Poggianti, B., et al. 2017, *A&A*, 599, A81
 Moretti, A., Poggianti, B. M., Fasano, G., et al. 2014, *A&A*, 564, A138
 Nelson, D., Pillepich, A., Genel, S., et al. 2015, *Astronomy and Computing*, 13, 12
 Pasquato, M. & Bertin, G. 2008, *A&A*, 489, 1079
 Press, W. H. & Schechter, P. 1974, *ApJ*, 187, 425
 Sciarra, M., Chiosi, C., D'Onofrio, M., & Cariddi, S. 2019, *ApJ*, 870, 70
 Shankar, F., Lapi, A., Salucci, P., De Zotti, G., & Danese, L. 2006, *ApJ*, 643, 14
 Shankar, F., Marulli, F., Bernardi, M., et al. 2011, ArXiv e-prints [arXiv:1105.6043]
 Shen, S., Mo, H. J., White, S. D. M., et al. 2003, *MNRAS*, 343, 978
 Somerville, R. S., Behroozi, P., Pandya, V., et al. 2018, *MNRAS*, 473, 2714
 Springel, V., White, S. D. M., Jenkins, A., et al. 2005, *Nature*, 435, 629
 Terrazas, B. A., Bell, E. F., Pillepich, A., et al. 2019, arXiv e-prints, arXiv:1906.02747
 Valentinuzzi, T., Fritz, J., Poggianti, B. M., et al. 2010, *ApJ*, 712, 226
 Valentinuzzi, T., Poggianti, B. M., Fasano, G., et al. 2011, *A&A*, 536, A34
 van Dokkum, P. G., Whitaker, K. E., Brammer, G., et al. 2010, *ApJ*, 709, 1018
 Varela, J., D'Onofrio, M., Marmo, C., et al. 2009, *A&A*, 497, 667
 Vogelsberger, M., Genel, S., Springel, V., et al. 2014a, *Nature*, 509, 177
 Vogelsberger, M., Genel, S., Springel, V., et al. 2014b, *MNRAS*, 444, 1518
 Warren, S., Lawrence, A., Almaini, O., et al. 2006, *The Messenger*, 126, 7
 Woo, J., Courteau, S., & Dekel, A. 2008, *MNRAS*, 390, 1453

Appendix A: The stellar-to-halo mass relation

The ratio M_s/M_D (and its inverse M_D/M_s) are key quantities in the calculation of the (half-mass or effective) radius of the stellar component of a galaxy, see eq.(10) of Sect. 4. The analysis of the Illustris data and the inspection of Tables B.1, B.2, and B.3 in Appendix B show that the ratios M_s/M_D and M_D/M_s in turn depend on the total mass of the galaxy and the redshift z_f at which the bulk of star formation occurs.

The dependence of the ratio M_s/M_D on M_D and redshift z for the Illustris data is shown in Fig. A.1. For low values of the redshift (say below 0.6), this ratio gently decreases with the mass M_D (low mass galaxies are slightly more efficient in building their stellar content); the opposite occurs for higher redshifts, where the ratio M_s/M_D increases with M_D , i.e. the stellar mass built-up in low mass galaxies is expected to be less than in the massive ones.

With the aid of the theoretical data for M_D and M_s presented in Sect.4, we derive an analytical expression interpolating the ratio $M_s/M_D(M_D, z)$ as function of M_D and z

$$\log \frac{M_s}{M_D} = [0.218z - 0.101] \log M_D + [0.169z - 2.227] \quad (\text{A.1})$$

where the halo mass goes from $10^4 M_\odot$ to $10^{14} M_\odot$ and the redshift from 0 to 4. The ratios M_s/M_D predicted by eq. (A.1) are indicated by the small black dots of Fig. A.1. The range of application of relation (A.1) is $0 \leq \log z \leq 4$.

Similar relationships for the ratio $m = M_D/M_s$ can be found in literature, see for instance Fan et al. (2010), Shankar et al. (2006), and more recently Girelli et al. (2020).

For $M_D \geq 10^{11} M_\odot$ Fan et al. (2010) propose the relation

$$m = \frac{M_D}{M_s} = 25 \left(\frac{M_D}{10^{12}} \right)^{0.1} \left(\frac{1+z}{4} \right)^{-0.25} \quad (\text{A.2})$$

from which we derive the ratio M_s/M_D shown in Fig. A.1 by the red circles. In practice there is no dependence on the redshift.

Remarkably, the Fan et al. (2010) curve agrees with the one we have derived from the Illustris models for values of the redshift smaller than about 1.6 (the slope is nearly identical).

Shankar et al. (2006, and references) present a detailed analysis of the dependence of M_s on M_D . First, they suggest that for $M_D < 10^{11} M_\odot$ the relation should be

$$m = \frac{M_D}{M_s} = C M_D^{-2/3} \quad (\text{A.3})$$

with C a suitable proportionality constant to be determined. By imposing equality between the values of m determined with the two above relationships at the transition mass $M_D \geq 10^{11} M_\odot$, the proportionality constant is $\log C = 9.044$. The ratios M_D/M_s predicted by eq.(A.3) are shown in Fig.A.1 by the dark golden circles. It is worth noting that the Shankar et al. (2006) relation agrees with that of the Illustris models for redshifts in the range from 2 to 4.

Amazingly, it is worth noting that in Fig. A.1 the linear extrapolation of the Fan et al. (2010) relationship (red golden circles) to lower masses and the linear extrapolation of the Shankar et al. (2006) curve (dark golden circles) to higher values of the mass encompass the theoretical predictions from the Illustris models for all the values of the redshift.

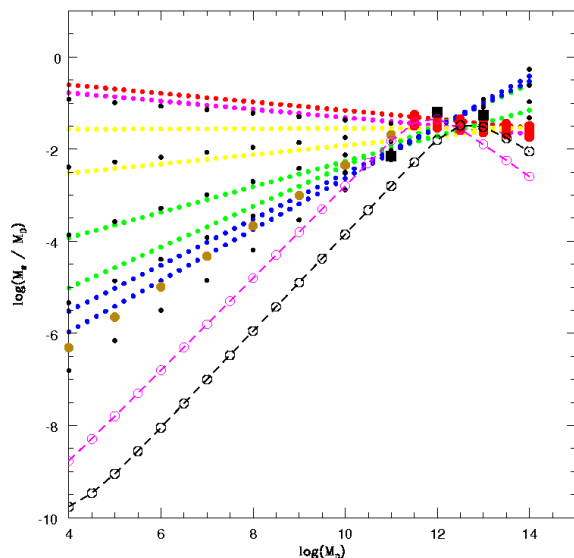


Fig. A.1. The relations M_s/M_D vs M_D at different redshifts for theoretical models. The dotted lines of different colors correspond to the eight values of the redshift $z=0$ and $z=0.2$ (top, red), $z=0.6$, $z=1.0$ (intermediate, yellow), $z=1.6$ and $z=2.2$ (intermediate, green), $z=3$ and to $z=4$ (bottom, blue). The black dots are the values predicted by eq. (A.1) at varying $\log M_D$ from 4 to 14 in steps of 1 and redshift z from 0 to 4 in steps of 1, respectively. The large red and golden circles are the combination of eq. (A.3) and eq. (A.2), respectively. The open magenta ($z=0$) and black ($z=3.95$) circles are relation M_s/M_D vs M_D at different redshifts according to Girelli et al. (2020). Note how all relations agree each other at $\log M_D \approx 12$ whereas they badly disagree each other at lower values of M_D . All masses are in solar units.

Second, Shankar et al. (2006) derive an analytical expression for the relation between M_s and M_D

$$M_s = 2.3 \times 10^{10} M_\odot \frac{(M_D/3 \times 10^{11} M_\odot)^{3.1}}{1 + (M_D/3 \times 10^{11} M_\odot)^{2.2}} \quad (\text{A.4})$$

for $M_D \geq 10^{11} M_\odot$. In this relation there is no explicit dependence on the redshift. The ratios M_s/M_D predicted by eq.(A.4) are shown in Fig. A.1 by the black filled squares. Eq. (A.4) predict ratios $m(M_D, z)$ that agree with those from eq.(A.1) derived from Illustris data, eq.(A.2) from Fan et al. (2010), and eq.(A.3) only in the region around $\log(M_D) \approx 12$ and $z \approx 0$.

In a very recent study Girelli et al. (2020) have thoroughly investigated the stellar-to-halo mass ratio of galaxies ($M_s/M_{DM} = 1/m$ in the mass interval $10^{11} < M_{DM} < 10^{15}$ and redshifts from $z = 0$ to $z = 4$). They use a statistical approach to link the observed galaxy stellar mass function on the COSMOS field to the halo mass function from the Λ CDM-Dustgrain simulation and derive an empirical model to describe the variation of the stellar-to-halo mass ratio as a function of the redshift. Finally they provide analytical expressions for the function $M_s(M_D, z)$. The relations M_s/M_D vs M_D as function of the redshift obtained with the formalism of Girelli et al. (2020) are also shown in Fig. A.1 (the magenta and dark-olive-green dots joined by solid lines of the same color) and are compared with the results of our study. See also for a similar analysis the study of Engler et al. (2020).

It is soon evident that while all studies agree on the M_s/M_D ratios for objects with halo mass in the interval $11.5 \leq \log M_D \leq 12.5$ nearly independently of the redshift, they badly disagree each other going to lower values of the halo mass. Furthermore,

they also disagree with the theoretical results predicted by Illustris.

To cope with this major point of uncertainty on the correct function $M_s(M_D, z)$, we prefer to provisionally simplify the whole issue and, basing on the results from the few galaxy models to disposal (at redshift $z = 0$ by construction), we derive the following dependence for the ratios M_s/M_D and its inverse $m = M_D/M_s$

$$\begin{aligned} \log \frac{M_s}{M_D} &= -0.062 \log M_D - 0.429 \\ \log \frac{M_D}{M_s} &= 0.062 \log M_D + 0.429 \end{aligned} \quad (\text{A.5})$$

that do not depend on the redshift. However, since eq. (10) in which the ratio $m(M_D, z)$ is used contains its own dependence of the redshift, the final results still depend on this important parameter.

Appendix B: Hydrodynamical models of ETGs

Appendix B.1: The pure monolithic scheme

Chiosi & Carraro (2002), by means of hydrodynamical simulations, incorporating radiative cooling, star formation, energy feed-back and chemical evolution, addressed the problem of the formation and evolution of ETGs (from dwarf to normal/giant systems) in the framework of the SCDM cosmological model of the Universe and monolithic scheme of galaxy formation. The cosmological parameters were $H_0 = 65 \text{ km s}^{-1} \text{ Mpc}^{-1}$, Baryonic to Dark Matter ratio 1 to 9, i.e. for $M_T = M_{BM} + M_{DM}$ $M_{BM} = 0.1M_T$ and $M_{DM} = 0.9M_T$, and the redshift at which galaxies were supposed to start the collapse ($z_f = 1$ and $z_f = 5$). A lump of mass (perturbation) with spherical symmetry whose density exceeds a critical value is let collapse toward the virial condition. A MonteCarlo procedure is adopted to fix the initial coordinates and velocities of the DM and BM particles. Table B.1 summarizes the key parameters and results of the models. The key results of this study are: (i) The duration, strength and shape of the star formation rate as function of time strongly depend on the galaxy mass and the initial density: (a) Galaxies of high initial density and total mass over an ample range undergo a prominent initial episode of SF ever since followed by quiescence. (b) The same applies to high mass galaxies of low initial density, whereas the low mass ones undergo a series of burst-like episodes that may stretch up to the present. The details of their SF history are also very sensitive to the value of the initial density.

(ii) The mass turned into stars per unit total mass of the galaxy is nearly constant which means that the engine at work is the same.

(iii) The ratio between the left-over gas to the initial total BM decreases at increasing total mass of the galaxy.

(iv) As a result of star formation in the central core of the galaxy and consequent gas heating, large amounts of gas are pushed to large distances. After cooling, part of the gas falls back towards the central furnace.

(v) Galactic winds occur. In general all galaxies are able to eject part of their gas content into the inter-galactic medium. However, the percentage of the ejected material increases at decreasing galaxy mass.

Appendix B.2: The hierarchical scheme

Merlin et al. (2010, 2012) with the aid of the parallel hydrodynamical code EvoL produced a number of models for ETGs with different mass and/or initial density (twelve cases in total).

The models were followed from the epoch of their detachment from the linear regime, i.e. $z_i \geq 20$, to a final epoch (redshift z_f) varying from model to model (however with $z_f \leq 1$). The simulations included radiative cooling down to 10 K, star formation, stellar energy feedback, re-ionizing photo-heating background, and chemical enrichment of the interstellar medium. The reader can refer to the cited papers for all the details on the method and the code in use as well as on model results.

The assumed cosmology was the standard Λ -CDM, with $H_0=70.1 \text{ km/s/Mpc}$, flat geometry, $\Omega_\Lambda=0.721$, $\sigma_8=0.817$; the baryonic fraction ≈ 0.1656 .

Each model starts as a sphere cut at certain redshift z_i from a wider cosmological simulation in which density fluctuations exist. At the center of the sphere there is a peak of given density contrast with respect to the cosmological background. The density contrast is measured by the quantity $[\delta\rho - 1] = [(\langle \rho \rangle - \rho_b)/\rho_b]$, where $\langle \rho \rangle$ is the mean density of the perturbation and ρ_b the density of the background. The central density peak has a given total mass M_T , sum of the DM and BM components. This is the proto-halo of our model galaxy in which stars will be formed at later times. The cosmological simulation provides the initial positions and velocities of all the particles in the proto-halo. An outward radial component is added to the velocity of each particle to take the expansion of the Universe into account. The initial conditions are set in such a way that each model is a re-scaled version of a single reference proto-galactic halo, with different total mass and/or initial over-density. The proto-galactic halos are then followed through their early stages of expansion following the Hubble flow, the turn around, and the collapse. The redshift at which the collapse begins varies from model to model and inside the same model from the center to the outer regions. In general the collapse occurs during the redshift interval $4 > z > 2$, it starts first in the central regions and gradually moves outwards. The collapse is complete at redshift $z \approx 2$. All the models develop a central stellar system, with a spheroidal shape. Massive halos ($M_T \approx 10^{13} M_\odot$) experience a single, intense burst of star formation (with rates $\geq 10^3 M_\odot/\text{yr}$) at early epochs, consistently with observations, with a less pronounced dependence on the initial over-density; intermediate mass halos ($M_T \approx 10^{11} M_\odot$) have star formation histories that strongly depend on their initial over-density, i.e. from a single peaked to a long lasting period of period of activity with strong fluctuations in the rate; finally small mass halos ($M_T \approx 10^9 M_\odot$) always have fragmented histories, resulting in multiple stellar populations, due to the so-called ‘‘galactic breathing’’ phenomenon. They confirm the correlation between the initial properties of the proto-halos and their star formation histories already found by Chiosi & Carraro (2002). The models have morphological, structural and photometric properties comparable to real galaxies, in general closely matching the observed data; there are minor discrepancies that are likely of numerical origin (see Merlin et al. 2012, for all other details). These models can be classified as *early hierarchical* because they undergo repeated episodes of mass accretion of sub-lumps of matter inside the original density contrast in very early epochs and essentially evolve in isolation ever since. These reference models are calculated adopting a star formation efficiency $\epsilon_{sf} = 1$. This value is larger than current estimates from observational

Table B.1. Summary of the properties of the hydrodynamical model galaxies by Chiosi & Carraro (2002). **Left–Initial conditions:** M_T is the total mass of the proto-galaxy, M_{DM} and M_{BM} the mass of DM and BM, respectively, R_{200} the initial radius, $\langle\rho\rangle$ the mean mass density. Masses are in M_\odot , radii in kpc, and densities in M_\odot/kpc^3 . **Middle–Final results:** the present day star M_s and gas M_g mass contents, the half-mass radius R_s and central velocity dispersion σ_s of the stellar mass, and half-mass radius R_{DM} and central velocity dispersion σ_{DM} of DM. **Right–Galactic winds:** $M_{g,esc}$ amount of gas inside the radius at which the radial velocity is equal to the escape velocity; $\Delta M_{g,w}$ amount of gas lost in the galactic wind; $\Delta M_{g,w}/M_g$ percentage of gas lost in the wind with respect to the amount left over by Star Formation. Masses are in M_\odot , radii in kpc, densities in M_\odot/kpc^3 , and velocity dispersions in km/s

Model	M_T	M_{DM}	M_{BM}	R_{200}	$\langle\rho\rangle_0$	M_s	M_g	R_s	σ_s	R_{DM}	σ_{DM}	$M_{g,esc}$	$\Delta M_{g,w}$	$\frac{\Delta M_{g,w}}{M_g}$
Models with mean initial density $\langle\rho\rangle \approx 200 \times \rho_u(z)$ with $z \approx 5$														
(1A)	1e13	9.0e12	1.0e12	83	4e6	6.4e11	3.6e11	1.87	530	25	646	1.5e11	2.1e11	58
(6A)	1e9	9.0e8	1.0e8	4	4e6	3.2e7	6.8e7	0.07	17	1	20	2.4e7	4.5e7	66
Models with mean initial density $\langle\rho\rangle \approx 5 \times \rho_u(z)$ with $z \approx 1$														
(1B)	5e13	4.5e13	5.0e12	681	4e4	4.4e12	0.6e12	29	365	276	654	4.0e11	2.0e11	33
(2B)	5e12	4.5e12	5.0e11	316	4e4	4.0e11	1.0e11	16	215	170	324	6.5e10	3.5e10	35
(3B)	1e12	9.0e11	1.0e11	184	4e4	6.4e10	3.6e10	9	98	63	153	1.9e10	1.7e10	47
(4B)	2e11	1.8e11	2.0e10	108	4e4	1.2e10	0.8e10	5	69	53	119	0.4e10	0.4e10	50
(5B)	1e10	9.0e9	1.0e9	40	4e4	4.0e8	6.0e8	2	33	19	55	2.5e8	3.5e8	58
(6B)-LD	1e9	9.0e8	1.0e8	35	5e3	1.3e7	8.7e7	9	3	1	13	1.5e7	0.8e7	35
(6B)-ID	1e9	9.0e8	1.0e8	19	4e4	2.5e7	7.5e7	1	6	10	15	3.0e7	4.5e7	60
(6B)-HD	1e9	9.0e8	1.0e8	16	6e4	7.7e7	2.3e7	0.3	5	19	19	6.4e7	2.3e7	24
(7B)	1e8	9.0e7	1.0e7	9	4e4	1.8e6	8.2e6	1	3	4	10	3.0e6	5.1e6	63

Table B.2. The early-hierarchical galaxy models by Merlin et al. (2010, 2012). Left to right: total initial mass $M_T = M_{DM} + M_{BM}$ [in units of $10^{12} M_\odot$], corresponding (initial) gas mass $M_{g,i}$ [in units of $10^{12} M_\odot$], redshift z_i at which the proto-halo is selected from the background in the cosmological grid, mean halo over-densities $(\langle\rho\rangle - \rho_b)/\rho_b = [\delta\rho - 1]_i$ (ρ_b is the background density) at the redshift z_i , initial proper physical radius of the halo [in kpc], redshift of the last computed model z_f , corresponding age t_f [in Gyr], virial radius of the whole system R_{vir} [in kpc], half-mass radius $R_{1/2}$ at z_f , and the total stellar mass M_s at the final redshift [in units of $10^{12} M_\odot$].

Model	M_T	$M_{g,i}$	z_i	$[\delta\rho - 1]_i$	R_i	z_f	t_f	R_{vir}	$R_{1/2}$	M_s
HDHM	17.5	2.90	46	0.12	97.17	0.22	11.0	153.0	15.6	0.75
MDHM	17.5	2.90	39	0.12	114.31	0.77	8.0	141.8	15.2	0.74
LDHM	17.5	2.90	33	0.12	134.49	0.50	8.7	133.8	14.1	0.73
VLDHM	17.5	2.90	23	0.12	194.34	0.83	6.6	112.5	10.8	0.63
HDMM	0.269	0.0445	54	0.11	20.99	1.0	5.8	37.6	5.5	0.020
MDMM	0.269	0.0445	45	0.11	24.69	0.75	7.0	35.7	5.4	0.019
LDMM	0.269	0.0445	38	0.11	29.05	0.58	8.1	33.3	4.8	0.019
VLDMM	0.269	0.0445	26	0.11	41.98	0.15	11.8	28.3	4.7	0.017
HDLM	0.00417	0.000691	63	0.09	4.48	0.36	9.7	9.2	2.3	0.00015
MDLM	0.00417	0.000691	53	0.09	5.27	0.22	11.0	10.0	2.1	0.00014
LDLM	0.00417	0.000691	45	0.09	6.20	0.05	13.0	11.8	2.0	0.00014
VLDLM	0.00417	0.000691	31	0.09	8.96	0.0	13.7	10.5	2.5	0.00010

data in the local Universe, i.e. $\epsilon_{sf} \approx 0.025$ (Lada & Lada 2003; Krumholz & Tan 2007), and theoretical considerations on the global star-to-total mass ratio in galaxies that suggest $\epsilon_{sf} \leq 0.1$. However, adopting a high value of ϵ_{sf} allows for a strong reduction of the computational time, while preserving the basic properties of the models (for a complete discussion see Merlin et al. 2012). The properties of all computed model galaxies are listed in Table B.2.

Using the same numerical code and approach for the initial conditions, Chiosi et al. (2012) produce a group of ancillary models, whose initial parameters and key results are listed in Table B.3. These models are calculated to explore the consequences of much higher initial density contrasts and/or lower star formation efficiencies ϵ_{sf} . The effect of the higher initial density is already known from the old calculations Chiosi & Carraro (2002) and the models by Merlin et al. (2012): galaxies of the same mass will be shifted on the MR-plane to smaller radii.

As expected by decreasing the efficiency ϵ_{sf} , star formation is delayed or even inhibited. The gas continues to flow into the gravitational potential well till the threshold density for star for-

mation to occur is reached and/or sufficient number of stars are formed, the newly born galaxy has much smaller dimension with respect to the corresponding object with higher efficiency of star formation.

All the ancillary models are calculated limited to the very early evolutionary stages, to show in the MR-plane the initial position of a model galaxy in which the gas content has reached densities much higher than the formal mean background density fixed by cosmology. The parameter f_δ indicates the factor by which the initial density of same model in the first group (Table B.2) is scaled. As already said in these models we also change the efficiency of star formation ϵ_{sf} as indicated in column (3) Table B.3. In a few models, indicated by ϵ_Z , the efficiency of star formation increases with metallicity Z . The efficiency goes from $\epsilon_{sf} = 0.1$ for $Z=0.0001$ to $\epsilon_{sf} = 1$ for $Z=0.01$ (close to the solar value). No special meaning must be given to this relation, it is simply meant to evaluate the effect of a star formation efficiency increasing with the metallicity. In any case, this effect plays a marginal role on the position of the model galaxies on the MR-plane, see the entries of Table B.3.

Table B.3. The ancillary models of Chiosi et al. (2012). The meaning of the symbols is as follows: Model is the two-letter string identifying the model according to the mass: MM for intermediate mass galaxy $2.69 \times 10^{11} M_{\odot}$ and LM for the low mass case $4.17 \times 10^9 M_{\odot}$; f_{δ} is the multiplicative factor of the initial over-density of the reference model of the same mass; ϵ_{sf} is the dimensionless efficiency of the star formation rate, the symbol ϵ_Z means that the efficiency is supposed to increase from $\epsilon_{sf} = 0.1$ for $Z=0.0001$ to $\epsilon_{sf} = 1$ for $Z=0.01$ (close to the solar value). All other symbols have the same meaning as in Table B.2.

Model	f_{δ}	ϵ_{sf}	M_t	M_{gi}	z_i	$[\delta\rho - 1]_i$	R_i	z_f	t_f	R_{vir}	$R_{1/2}$	M_s
MM	20	1	0.269	0.0445	181	0.18	6.3	62.0	0.04	1.8	0.63	0.010
MM	20	1	0.269	0.0445	181	0.18	6.3	30.4	0.10	4.9	1.26	0.054
MM	20	0.1	0.269	0.0445	181	0.18	6.3	56.0	0.04	2.1	0.08	0.0050
MM	20	0.1	0.269	0.0445	181	0.18	6.3	49.0	0.05	2.6	0.08	0.0074
MM	20	ϵ_Z	0.269	0.0445	181	0.18	6.3	59.0	0.04	2.0	0.07	0.0036
MM	20	ϵ_Z	0.269	0.0445	181	0.18	6.3	46.0	0.05	2.9	0.09	0.0083
MM	15	1	0.269	0.0445	140	0.18	8.2	30.4	0.10	4.5	1.08	0.026
MM	12	1	0.269	0.0445	117	0.17	9.8	30.4	0.10	4.1	0.92	0.011
MM	12	1	0.269	0.0445	117	0.17	9.8	18.8	0.20	7.4	0.98	0.015
MM	12	ϵ_Z	0.269	0.0445	117	0.17	9.8	36.0	0.08	3.1	0.07	0.0032
MM	12	ϵ_Z	0.269	0.0445	117	0.17	9.8	30.4	0.10	4.2	0.10	0.00575
MM	5	1	0.269	0.0445	68	0.14	16.7	7.0	0.70	19.2	5.75	0.019
MM	5	1	0.269	0.0445	68	0.14	16.7	4.1	1.50	34.3	6.76	0.057
LM	20	1	0.00417	0.000691	112	0.16	2.6	25.3	0.13	1.2	0.32	0.00016
LM	20	1	0.00417	0.000691	112	0.16	2.6	18.8	0.20	1.8	0.31	0.00017
LM	20	0.1	0.00417	0.000691	112	0.16	2.6	25.4	0.13	1.3	0.02	0.000091